MRI based Electrical Properties Tomography

Electromagnetic inversion

P. S. Fuchs

Technische Universiteit Delft

TU Delft

MRI based Electrical Properties Tomography

Electromagnetic inversion

by

P. S. Fuchs

to obtain the degree of Master of Science
at the Delft University of Technology,
to be defended publicly on Tuesday June 28, 2016 at 10:45 AM.

Student number:	1527436	
Project duration:	September 1, 2015 – June 28, 2016	
Thesis committee:	Prof. dr. ir. A. -J. van der Veen,	TU Delft, Responsible Professor
	Dr. ir. R. F. Remis,	TU Delft, supervisor
	Prof. dr. ir. A. G. Webb,	LUMC
	Dr. ir. C. A. T. van den Berg,	UMC Utrecht

This thesis is confidential and cannot be made public until June 31, 2017.

The cover image is a simulated B_1^- field of a pelvis slice from the Ella model (ITIS Foundation [6]).
An electronic version of this thesis is available at `http://repository.tudelft.nl/`.

TU Delft

Abstract

In magnetic resonance imaging (MRI) the interest in electric properties tomography (EPT) is growing. In current EPT applications the reconstruction is performed based on the Helmholtz equation which relies on the assumption of a homogeneous contrast. The goal of this thesis is to present new approaches to reconstruct the electrical properties that require less assumptions on the contrast.

Two fundamentally new approaches are presented, one based on first order differentiation and one on the global integral field equations using a contrast-source variable. In this thesis these methods are described alongside the existing Helmholtz based approach, the contrast source inversion (CSI) - EPT approach, and a deconvolution approach.

Reconstruction of both two- and three-dimensional simulations as well as the reconstruction of an in vivo measurement are performed to compare the five different methods.

It can be concluded from this comparison that methods that are not based on the homogeneous contrast assumption are much more accurate (overal) than the Helmholtz equation based method. Both CSI and the direct inversion method based on the global integral equations perform comparable, but the latter is significantly faster and offers almost the same range of flexibility regarding regularisation and preconditioning. The direct inversion method is an improvement on the deconvolution method, performing equally well regarding noise robustness, but offering better reconstructions in all cases due to the lack of an apodisation step. The first order differential method provides a surprisingly robust, accurate, and extremely fast way to get insight into the data, and shows that the inversion problem in MRI is actually very well behaved as far as inversion problems go.

These new methods provide new insight into the inversion problem in MRI, specifically for EPT and get us one step closer to accurate electric properties reconstruction from an MRI scan.

Preface

In this thesis the work of almost a year of research into inversion methods for MRI applications is presented.

With a solid background in numerical methods I have approached Rob Remis as early as the fall of 2014 to discuss possibilities of doing a thesis project with him. Back then already, the CSI-EPT method was being worked on jointly between him and (amongst others) Edmond Balidemaj, and they had some exciting results.

Quickly Rob's enthusiasm on the subject spoke to me, and by December 2014 I had decided I definitely wanted to get involved in the MRI research. (Unfortunately) it wasn't until September 2015 that I finally started this research, due to some planned travels abroad. To see the sights, before settling back down in Delft was the plan.

From that point onward the process was equally convoluted as the buildup towards it, from working on an amplitude-only approach, through various other reconstruction ideas that came up during the research, to finding out that phase-only would be a much better way to go…

Nothing turned out quite as it was planned, but I daresay that in the end it turned out much better and I hope you enjoy reading about the discoveries that were made as much as I enjoyed writing about them.

Much is yet to be researched and said on this subject, and I do hope I have the opportunity to continue my voyage of discovery.

P. S. Fuchs
Delft, June 2016

Acknowledgements

Of course a thesis like this could never have come about without the help of a lot of wonderful and talented people.

Many comments from the MRI community have helped me gain insight into the workings of MRI, and understanding of the physics and mathematics behind it. Many thanks to Jeroen, Wyger, Rita, Stefano, and Edmond for helping me out, from simple scaling issues of operators, to antenna settings in real scans. I also like to thank Andrew Webb and Nico van den Berg for their direct and indirect comments, and for taking the time to take part in my thesis committee.

Then there are the people I have spent most of my time with, my roommates, and my partner in crime Daan, whom I wish much luck in London, although I'll be missing his coffee-break presence, and inspiring work ethic. It was wonderful being able to share the struggles of research with someone encountering the same. Also my fellow German Jörn, without whom my numerical computer-fu wouldn't be nearly as good as it is (also thanks for letting me stay in your room).

At the Circuits and Systems department I would not have had such a good time without the technical support from Antoon, and the great spirit and organisational skills of Minakshie, who have helped me with all my small struggles, arranging meetings and fixing drivers, thanks a lot!

Last but certainly not least, my most important colleague during my masters' thesis project has to be my supervisor Rob. Rob, thanks so much for taking the time and sparring with me, reviewing my work and coming up with novel ideas to be tried all the time, and getting me introduced to the whole MRI 'world' in Holland.

Contents

1 Introduction

Medical imaging is a dynamic field. It contains some of the most versatile diagnostic techniques available to doctors. In magnetic resonance imaging (MRI) the interest in electric properties tomography (EPT) is growing. This is the process of estimating the electrical properties (conductivity and permittivity) of tissue using the measured magnetic field.

In the current EPT methods, the reconstruction is performed using the Helmholtz approximation [20]. The goal of this thesis is to present new approaches to reconstruct the electrical properties that require less assumptions on the to be reconstructed contrast.

First a short introduction on MRI and EPT will be given in Section 1.1. After this a description of the electromagnetic (EM) fields inside a scanner and their interaction will be given in Chapter 2. There a scattering formalism is derived and from it the various inversion algorithms which are described in Chapter 3. Following this reconstruction results are displayed in Chapter 5. At the end based on these results the assumptions are discussed in Chapter 6 after which the conclusions of this research are given in Chapter 7.

1.1. How does magnetic resonance imaging work?

Magnetic Resonance Imaging (MRI) is a way to image the inside of the human body through the magnetic resonance effect. The magnetic resonance effect, which will be described below, was first discovered by Paul C. Lauterbur in 1971 [7]. Its application to tomography (mapping the human body) has been developed since then and a large number of commercial MRI machines are available nowadays.

MRI uses the signal from the nuclei of basic hydrogen atoms ($^1\mathrm{H}$) to generate an image. To understand how this works, quantum mechanics is necessary. It can however be explained using a macroscopic example. You can imagine the nucleus of a hydrogen atom as a spinning top. This spinning is an intrinsic property of elementary particles. Through this spinning a magnetic moment is induced. A magnetic moment means that it acts like a magnet with a plus and minus pole.

Now, water ($\mathrm{H_2O}$), which constitutes about 70% of your bodies mass, contains a lot of hydrogen atoms. In an MRI scanner a large external magnetic field is applied to the body. This magnetic field (like the magnetic field of the earth acts on a compass) aligns the nuclear spins.

To generate an image in these conditions, an electromagnetic pulse (or a series of pulses) is emitted by an external antenna. The frequency of this pulse is chosen so that the electromagnetic energy excites the spin transitions. This means the EM pulse pushes the spinning nuclei out of alignment. As the spins return to equilibrium (which is called relaxing) they emit

radio-waves themselves depending on the external magnetic field. These emitted waves are then measured and translated into an MRI image.[1]

1.1.1. Electric Properties Tomography

A special application of MRI measurements is the so called EPT. This is a relatively new process, the goal of which is to reconstruct the electric properties of the human tissue scanned (conductivity and permittivity) [10]. Most electric property (EP) methods are based on the well-known B1 mapping, as are the methods described in this thesis. A single RF coil of a standard MR system is sufficient for this approach.

The electric properties of the human body characterise a number of healthy and pathological tissue. They can also be used to determine the specific absorption rate (SAR) of the tissue. The SAR is needed to calculate how much the tissue will heat up in a scan. This is used in medical procedures such as hyperthermia, and can also help keep patients safe from unwanted heating up during MRI scans.

1.2. What is inversion?

In physics, models are often used to generate synthetic data for various applications such as simulations. This is called solving a forward problem. If, however, we are interested in the reverse, finding model parameters from data, it is called an inversion problem.

Often these inversion problems are ill posed, and in addition measured data is inaccurate and incomplete making the problem hard to solve.

There are two types of inverse problems, which are very much related. One is the inverse source problem, where the goal is to reconstruct a source given a measured field. The second is the inverse scattering problem, where the goal is to reconstruct medium properties inside the scattering object based on a measured field with a known source.

MRI revolves around the second type of problem, as the measured field is inside the body, or source. We will treat a generic formulation for the Maxwell equations which are fundamental to this problem later and then describe the MRI specifics.

[1] For a more thorough explanation see: `http://www.howequipmentworks.com/mri_basics/` (visited March 2016)

2

Electromagnetic theory

In this chapter the basic equations for EM fields in an MRI setting are defined and derived. With this a scattering formalism is described and the corresponding integral field equations are derived. These equations serve as a starting point for the inversion methods to be discussed in the following chapters.

2.1. Maxwell's equations

To begin the derivation of the field equations governing the working of an MRI scanner, we start with Maxwell's equations. The *local form* of Maxwell's equations *in matter* and in vector notation are

$$-\nabla \times \mathbf{H} + \mathbf{J}^{\mathrm{con}} + \partial_t \mathbf{D} = -\mathbf{J}^{\mathrm{ext}}, \tag{2.1}$$

$$\nabla \times \mathbf{E} + \partial_t \mathbf{B} = -\mathbf{K}^{\mathrm{ext}}. \tag{2.2}$$

The right-hand side of these equations are the sources feeding the fields, $\mathbf{J}^{\mathrm{ext}}$ and $\mathbf{K}^{\mathrm{ext}}$ are the external electric and magnetic currents flowing through, for example, an antenna, or in this case the MRI coil. These sources excite a field, which is described in the two main unknowns, namely the the magnetic field strength $\mathbf{H}$ and electric field strength $\mathbf{E}$. The remaining variables, $\mathbf{J}^{\mathrm{con}}$ is the volume density of the electric conduction current and $\mathbf{D}$ is the electric and $\mathbf{B}$ the magnetic flux density, are related to these field quantities through the constitutive relations. Through these relations $\mathbf{J}^{\mathrm{con}}$ and $\mathbf{D}$ depend *linearly* and in a *time-invariant* manner on the electric field $\mathbf{E}$ and $\mathbf{B}$ depends *linearly* and *time invariant* on the magnetic field $\mathbf{H}$. These dependencies are further defined in the frequency domain.

2.1.1. Frequency domain

In this thesis only *linear*, *causal* and *time invariant*[1] media are considered. Therefore it is possible to transform the above equations into the frequency domain. This allows the description of the steady state behaviour of single-frequency harmonic wave fields. The complex phasor $\hat{\mathbf{E}}(\mathbf{x}, \omega)$ (the over hat is used to denote the frequency domain representation of the quantities) relates to the time dependent $\mathbf{E}(\mathbf{x}, t)$ field quantity through a common time factor $e^{\mathrm{j}\omega t}$ as

$$\mathbf{E}(\mathbf{x}, t) = \Re\left\{\hat{\mathbf{E}}(\mathbf{x}, \omega) e^{\mathrm{j}\omega t}\right\}, \tag{2.3}$$

where j is the imaginary unit ($\mathrm{j}^2 = -1$). The location of the field is denoted by a vector $\mathbf{x} \in \mathbb{R}^3$ and the time or angular frequency are denoted by t and ω, respectively. The constitutive

[1] within the time of a measurement

relations in the frequency domain are then defined as

$$\hat{\mathbf{J}}^{\mathrm{con}}(\mathbf{x},\omega) = \hat{\sigma}(\mathbf{x},\omega)\hat{\mathbf{E}}(\mathbf{x},\omega), \tag{2.4}$$

$$\hat{\mathbf{D}}(\mathbf{x},\omega) = \hat{\varepsilon}(\mathbf{x},\omega)\hat{\mathbf{E}}(\mathbf{x},\omega), \tag{2.5}$$

$$\hat{\mathbf{B}}(\mathbf{x},\omega) = \hat{\mu}(\mathbf{x},\omega)\hat{\mathbf{H}}(\mathbf{x},\omega), \tag{2.6}$$

where $\hat{\sigma}, \hat{\varepsilon}, \hat{\mu}$ are the conductivity, permittivity and permeability. In the Maxwell equations, the time derivative becomes a multiplication with $\mathrm{j}\omega$ in the frequency domain, so the Equations (2.1) and (2.2) simplify to

$$-\nabla \times \hat{\mathbf{H}} + \hat{\eta}\hat{\mathbf{E}} = -\hat{\mathbf{J}}^{\mathrm{ext}}, \tag{2.7}$$

$$\nabla \times \hat{\mathbf{E}} + \hat{\zeta}\hat{\mathbf{H}} = -\hat{\mathbf{K}}^{\mathrm{ext}}, \tag{2.8}$$

where

$$\hat{\zeta}(\mathbf{x},\omega) = \mathrm{j}\omega\hat{\mu}(\mathbf{x},\omega), \tag{2.9}$$

$$\hat{\eta}(\mathbf{x},\omega) = \hat{\sigma}(\mathbf{x},\omega) + \mathrm{j}\omega\hat{\varepsilon}(\mathbf{x},\omega), \tag{2.10}$$

are the medium parameters, derived by substituting the constitutive relations into the Maxwell equations in the frequency domain.

2.2. Polarisation

Expanding the rotation in Maxwell's equations gives

$$\nabla \times \hat{\mathbf{H}} = \begin{pmatrix} \partial_y \hat{H}_z - \partial_z \hat{H}_y \\ \partial_z \hat{H}_x - \partial_x \hat{H}_z \\ \partial_x \hat{H}_y - \partial_y \hat{H}_x \end{pmatrix}. \tag{2.11}$$

The same also holds for the electric field component. Inside an MRI scanner, which can be considered a tube, in the middle of this tube, one direction of the geometry (and the field) is *translation invariant* (co-axial). The radiofrequency (RF) field excited by the coil is also constructed in a way to be translation invariant along this axis. This axis is chosen to be the z-axis by convention. Therefore, the z-dimension is *translation invariant* in this region and it is reasonable to assume $\partial_z H_i = 0$ for $i = [x, y, z]$. Updating the rotation with this assumption, we obtain

$$\nabla \times \hat{\mathbf{H}} = \begin{pmatrix} \partial_y \hat{H}_z \\ -\partial_x \hat{H}_z \\ \partial_x \hat{H}_y - \partial_y \hat{H}_x \end{pmatrix}. \tag{2.12}$$

Here something interesting can be observed. In the first of Maxwell's equations, the x and y components of the left-hand side (first and second terms of the vector) only contain the z-component of the magnetic field $\mathbf{H}$ (and x and y components of the electric field). In the second of Maxwell's equations these electric field components only occur in the z component of the left-hand side (and the z component of the H-field). The same is true vice versa for the x and y components of the H-field and z component of the E-field. In a two-dimensional setting, this allows the decoupling of the electromagnetic waves into E- and H-polarised waves as

$$\text{E-polarised:} \quad \{\hat{H}_x, \hat{H}_y, \hat{E}_z\}(x,y) \neq 0, \tag{2.13}$$

$$\text{H-polarised:} \quad \{\hat{E}_x, \hat{E}_y, \hat{H}_z\}(x,y) \neq 0, \tag{2.14}$$

where (x, y) is used to denote the position and the subscripts are used to denote the field components. A two-dimensional approximation is reliable inside the pelvic region (region occupied by the pelvis when a person is fully inside a scanner) that is situated in the mid-plane of generic 3T and 7T body coils [18].

This decouples the fields and lets us rewrite Maxwell's equations as

E-polarisation:

$$\partial_y \hat{H}_x - \partial_x \hat{H}_y + \hat{\eta}\hat{E}_z = -\hat{J}_z^{\text{ext}}, \tag{2.15}$$

$$\begin{pmatrix} \partial_y \\ -\partial_x \end{pmatrix} \hat{E}_z + \hat{\zeta} \begin{pmatrix} \hat{H}_x \\ \hat{H}_y \end{pmatrix} = -\begin{pmatrix} \hat{K}_x^{\text{ext}} \\ \hat{K}_y^{\text{ext}} \end{pmatrix}, \tag{2.16}$$

H-polarisation:

$$\begin{pmatrix} -\partial_y \\ \partial_x \end{pmatrix} \hat{H}_z + \hat{\eta} \begin{pmatrix} \hat{E}_x \\ \hat{E}_y \end{pmatrix} = -\begin{pmatrix} \hat{J}_x^{\text{ext}} \\ \hat{J}_y^{\text{ext}} \end{pmatrix}, \tag{2.17}$$

$$\partial_x \hat{E}_y - \partial_y \hat{E}_x + \hat{\zeta}\hat{H}_z = -\hat{K}_z^{\text{ext}}. \tag{2.18}$$

2.3. Sources

An E-polarised wave can be excited by electric current $\hat{J}_z^{\text{ext}}$ or magnetic currents $\hat{K}_x^{\text{ext}}$ and $\hat{K}_y^{\text{ext}}$, and an H-polarised wave can be excited by magnetic currents $\hat{K}_z^{\text{ext}}$ or electric currents $\hat{J}_x^{\text{ext}}$ and $\hat{J}_y^{\text{ext}}$. Given the coil setup along the z axis as described above, and an electric current being run through the coil along this axis, in this thesis E-polarised waves are considered without magnetic sources. Removing the magnetic current source term $\mathbf{K}^{\text{ext}}$, Equation (2.16) can be rewritten as

$$\begin{pmatrix} \hat{H}_x \\ \hat{H}_y \end{pmatrix} = -\frac{1}{\hat{\zeta}} \begin{pmatrix} \partial_y \\ -\partial_x \end{pmatrix} \hat{E}_z. \tag{2.19}$$

2.4. Scattering formalism

The problem is reformulated to better describe the *inhomogeneous* problem as it exists in the MRI case.

To begin, the *inhomogeneities* of the medium are confined to a *bounded* domain, which is called the object domain $\mathcal{D}$. This domain is embedded in an *unbounded, homogeneous* background medium, here denoted by $\mathcal{B}$.

Furthermore, the sources are located in the source domain $\mathcal{S}$, which is located in the background medium exterior to $\mathcal{D}$. This configuration (geometrically displayed as in an MRI scanner in 2D, but this does not have to be the case for the equations to hold) can be seen in Figure 2.1.

An additional set of equations for the background fields $\{\mathbf{E}^{\text{b}}, \mathbf{H}^{\text{b}}\}$ is added to the system formulation. These are the fields that would be present when there is no object $\mathcal{D}$.

Now rewriting the total field as the sum of the *background* field and the additional *scattered* field $\{\mathbf{E}^{\text{sc}}, \mathbf{H}^{\text{sc}}\}$ that is introduced by the object $\mathcal{D}$, such that

$$\hat{\mathbf{E}} = \hat{\mathbf{E}}^{\text{b}} + \hat{\mathbf{E}}^{\text{sc}}, \tag{2.20}$$

$$\hat{\mathbf{H}} = \hat{\mathbf{H}}^{\text{b}} + \hat{\mathbf{H}}^{\text{sc}}. \tag{2.21}$$

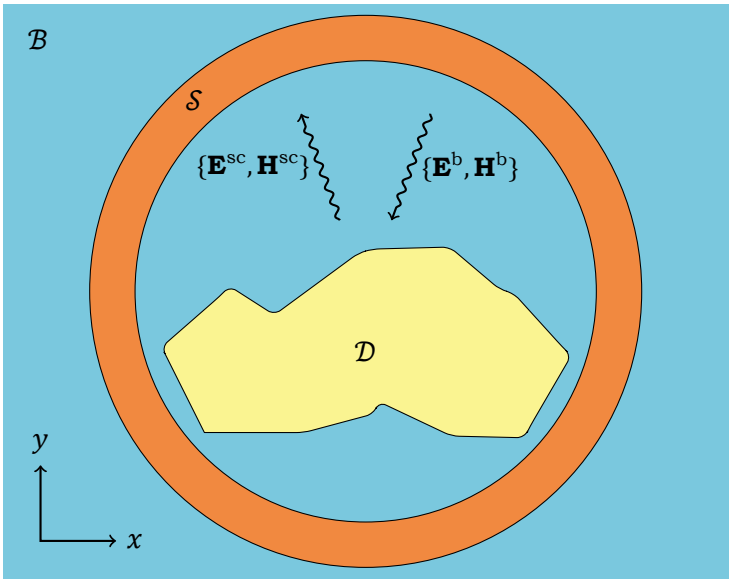

Figure 2.1: The general scattering configuration in an MRI scanner in 2D. The object domain is $\mathcal{D}$ and the source domain $\mathcal{S}$.

Since the sources for the total field and the background field remain the same, the background field can be written as

$$-\partial_y \hat{H}_x^{\mathrm{b}} + \partial_x \hat{H}_y^{\mathrm{b}} + \hat{\eta}_{\mathrm{b}} \hat{E}_z^{\mathrm{b}} = -\hat{J}_z^{\mathrm{ext}} \tag{2.22}$$

$$\begin{pmatrix} \partial_y \\ -\partial_x \end{pmatrix} \hat{E}_z^{\mathrm{b}} + \hat{\zeta}_{\mathrm{b}} \begin{pmatrix} \hat{H}_x^{\mathrm{b}} \\ \hat{H}_y^{\mathrm{b}} \end{pmatrix} = 0 \tag{2.23}$$

This allows us to relate the scattered field to the total field by subtracting Equation (2.23) from Equation (2.16) and Equation (2.22) from Equation (2.15). The new set of equations is

$$-\partial_y \hat{H}_x^{\mathrm{sc}} + \partial_x \hat{H}_y^{\mathrm{sc}} + \hat{\eta}_{\mathrm{b}} \hat{E}_z^{\mathrm{sc}} = -\hat{\eta}_{\mathrm{b}} \hat{\chi}_{\mathrm{e}} \hat{E}_z, \tag{2.24}$$

$$\begin{pmatrix} \partial_y \\ -\partial_x \end{pmatrix} \hat{E}_z^{\mathrm{sc}} + \hat{\zeta}_{\mathrm{b}} \begin{pmatrix} \hat{H}_x^{\mathrm{sc}} \\ \hat{H}_y^{\mathrm{sc}} \end{pmatrix} = -\hat{\zeta}_{\mathrm{b}} \hat{\chi}_{\mathrm{m}} \begin{pmatrix} \hat{H}_x \\ \hat{H}_y \end{pmatrix}. \tag{2.25}$$

Here the (contrast) variables

$$\hat{\chi}_{\mathrm{m}} = \frac{\hat{\zeta}(\mathbf{x}, \omega) - \hat{\zeta}_{\mathrm{b}}(\omega)}{\hat{\zeta}_{\mathrm{b}}(\omega)} \quad \text{and} \quad \hat{\chi}_{\mathrm{e}} = \frac{\hat{\eta}(\mathbf{x}, \omega) - \hat{\eta}_{\mathrm{b}}(\omega)}{\hat{\eta}_{\mathrm{b}}(\omega)} \tag{2.26}$$

have been introduced. Interesting to note is that the left-hand sides of Equations (2.24) and (2.25) describe the EM wave in a *homogeneous* medium. The same applies to the background fields, as the background medium is homogeneous.

One more simplification can be done before putting it all together. In the MRI setting it has been observed that the relative permeability variations of biological tissue are small [19]. These will therefore be ignored, by setting $\hat{\zeta}_b = \hat{\zeta}$, and consequently $\hat{\chi}_m = 0$. Equation (2.25) then simplifies to

$$\begin{pmatrix} \hat{H}_x^{\mathrm{sc}} \\ \hat{H}_y^{\mathrm{sc}} \end{pmatrix} = -\frac{1}{\hat{\zeta}_{\mathrm{b}}} \begin{pmatrix} \partial_y \\ -\partial_x \end{pmatrix} \hat{E}_z^{\mathrm{sc}}. \tag{2.27}$$

2.4.1. Homogeneous medium

To solve the system of equations described above, first the homogeneous case is considered. Substituting Equation (2.19) into Equation (2.15) and assuming a *homogeneous* medium (i.e.

$\hat{\zeta}$ does not depend on $\mathbf{x} \rightarrow \hat{\zeta}(\mathbf{x}, \omega) = \hat{\zeta}(\omega)$) leads to the second order differential equation

$$\left[\frac{1}{\hat{\zeta}}\left(\partial_y^2 + \partial_x^2\right) + \hat{\eta}\right]\hat{E}_z = -\hat{J}_z^{\text{ext}}. \tag{2.28}$$

Multiplying both sides with $\hat{\zeta}$ and introducing wave speed $\hat{k}^2 = -\hat{\eta}\hat{\zeta}$ gives

$$\left[\left(\partial_y^2 + \partial_x^2\right) - \hat{k}^2\right]\hat{E}_z = \frac{\hat{k}^2}{\hat{\eta}}\hat{J}_z^{\text{ext}}. \tag{2.29}$$

The equation can be simplified by applying a spatial Fourier transform. This transforms the derivatives (∇) into multiplications by $-\mathrm{j}\mathbf{k}$, where $\mathbf{k} = \mathbf{x}k_x + \mathbf{y}k_y + \mathbf{z}k_z$ is the angular wave vector.

Angular wave domain

In the angular wave domain Equation (2.29) becomes

$$\left(\mathbf{k}\cdot\mathbf{k} - \hat{k}^2\right)\tilde{E}_z = \frac{\hat{k}^2}{\hat{\eta}}\tilde{J}_z^{\text{ext}}. \tag{2.30}$$

where a tilde is used to denote the spatially and temporally transformed field quantities. Also $\mathbf{k}\cdot\mathbf{k}$ is the angular wave transform of the spatial derivative $\partial_x^2 + \partial_y^2$. The expression in front of $\tilde{E}_z$ is a *scalar, nonzero* factor. This expression leads to the introduction of the Green's function $\tilde{G}(\mathbf{k}, \omega)$ in the angular wave vector domain as

$$\tilde{G}(\mathbf{k}, \omega) = \frac{1}{\mathbf{k}\cdot\mathbf{k} - \hat{k}^2}. \tag{2.31}$$

Multiplying both sides by it yields

$$\tilde{E}_z = \tilde{G}(\mathbf{k}, \omega)\frac{\hat{k}^2}{\hat{\eta}}\tilde{J}_z^{\text{ext}}. \tag{2.32}$$

Before going back to the frequency domain the angular wave domain solution is simplified by introducing the vector potential

$$\tilde{A}(\mathbf{k}, \omega) = \frac{1}{\hat{\eta}}\tilde{G}(\mathbf{k}, \omega)\tilde{J}_z^{\text{ext}}, \tag{2.33}$$

which is also the point-source solution of the inhomogeneous Helmholtz equation in the angular wave domain.

Transforming the field expressions gives the frequency domain solution

$$\tilde{E}_z = \hat{k}^2\tilde{A} \quad \xrightarrow{\mathcal{F}_{\mathbf{k}}^{-1}} \quad \hat{E}_z = \hat{k}^2\hat{A}. \tag{2.34}$$

The inverse-transform of the vector potential results in a convolution

$$\hat{A}(\mathbf{x}, \omega) = \frac{1}{\hat{\eta}}\int_{\mathbf{x}'\in\mathbb{R}^2} \hat{G}(\mathbf{x} - \mathbf{x}', \omega)\hat{J}_z^{\text{ext}}(\mathbf{x}')\,\mathrm{d}V. \tag{2.35}$$

The Green's function $\hat{G}(\mathbf{x}, \omega)$ in the frequency domain will be discussed later.

2.5. Integral equations

To put it all together, a system of integral equations from which the total field can be found is constructed. Using the solution for the homogeneous contrast Equation (2.34), the background field can be written as

$$\hat{E}_z^{\mathrm{b}} = \frac{\hat{k}_b^2}{\hat{\eta}_{\mathrm{b}}} \int_{\mathbf{x}' \in \mathbb{R}^2} \hat{G}(\mathbf{x} - \mathbf{x}', \omega) \hat{J}_z^{\mathrm{ext}}(\mathbf{x}') \, \mathrm{d}V. \tag{2.36}$$

The same derivation can be applied to the scattered fields (with the contrast-source term $(\hat{\eta}_{\mathrm{b}} \hat{\chi}_{\mathrm{e}} \hat{E}_z)$ as the 'external' source). This leads to

$$\hat{E}_z^{\mathrm{sc}} = \hat{k}_b^2 \int_{\mathbf{x}' \in \mathcal{D}} \hat{G}(\mathbf{x} - \mathbf{x}', \omega) \hat{\chi}_{\mathrm{e}} \hat{E}_z(\mathbf{x}') \, \mathrm{d}V. \tag{2.37}$$

Note that the domain of integration is restricted to the (inhomogeneous) contrast, as outside of it the contrast term vanishes $(\hat{\chi}_{\mathrm{e}} = 0)$. Combining this with the definition of the total field gives

$$\hat{E}_z^{\mathrm{b}} = \hat{E}_z - \hat{k}_b^2 \int_{\mathbf{x}' \in \mathcal{D}} \hat{G}(\mathbf{x} - \mathbf{x}', \omega) \hat{\chi}_{\mathrm{e}} \hat{E}_z(\mathbf{x}') \, \mathrm{d}V. \tag{2.38}$$

This is an equation in terms of the total field, which will, as will later be shown allow the reconstruction of the contrast term (χ_{e}) from a measured field and known background field.

2.6. Measured field

The actual measured field in an MRI scanner is the B_1^+ field. This is related to the magnetic field as

$$\hat{B}_1^{\mathrm{sc};+} \equiv \frac{\hat{\mu}_{\mathrm{b}}}{2} \left[\hat{H}_x^{\mathrm{sc}}(\mathbf{x}) + \mathrm{j} \hat{H}_y^{\mathrm{sc}}(\mathbf{x}) \right]. \tag{2.39}$$

Here $\hat{H}_{x,y}$ is used to denote the different components of the $\hat{\mathbf{H}}$ vector (in the (x, y) directions). Note that it only depends on the *scattered* magnetic field, where the total B field would obviously depend on the total field.

2.7. Green's function

To solve the scattering equations posed before the Green's function as it was found in the angular wave domain needs to be transformed to the frequency domain. This yields, with $\hat{k} = \hat{k}_b$

$$\hat{G}(\mathbf{x}) = -\frac{\mathrm{j}}{4} H_0^{(2)}(\hat{k}_b |\mathbf{x}|) \tag{2.40}$$

Here $H_0^{(2)}$ is the Hankel function of the second kind and order zero [2, §11.4, p. 604-610].

3

Inversion Methods

In this chapter the inversion methods used to reconstruct the contrast (and electric field) from a measured B_1^+ field are described. First the methods based on the integral equations (global, or contrast-source) approach will be described, then the differentiation (local) approaches.

From this point on the over-hat ($\hat{\cdot}$) is dropped and all operations and variables are in the frequency domain unless otherwise stated.

3.1. Integral approach

As can be seen in Equation (2.37), the electric scattered field relies on the source term $\chi_\mathrm{e} E_z$. This term will be referred to as the contrast-source and denoted by w. Also, the contrast will be written without a subscript ($\chi = \chi_\mathrm{e}$) in the rest of this thesis, as no magnetic contrast is present. Explicitly we have

$$w(\mathbf{x}, \omega) = \chi(\mathbf{x}, \omega) E_z(\mathbf{x}), \tag{3.1}$$

and Equation (2.37) becomes

$$E_z(\mathbf{x}, \omega) = E_z^\mathrm{b}(\mathbf{x}) + k^2 \int_{\mathbf{x}' \in \mathcal{D}} G(\mathbf{x} - \mathbf{x}') w(\mathbf{x}', \omega) \, \mathrm{d}V. \tag{3.2}$$

Using the contrast-source, Equations (2.27) and (2.37), the $B_1^{\mathrm{sc};+}$ equation can be rewritten as

$$\hat{B}_1^{\mathrm{sc};+} = -\frac{\mu_\mathrm{b} k_\mathrm{b}^2}{2\zeta_\mathrm{b}} \left(\partial_y + \mathrm{j}\partial_x\right) \int_{\mathbf{x}' \in \mathcal{S}} G(\mathbf{x} - \mathbf{x}') w(\mathbf{x}', \omega) \, \mathrm{d}V. \tag{3.3}$$

The domain $\mathcal{S}$ is the domain in which the field is measured (in this case it is equal to the contrast domain $\mathcal{D}$). These are two equations with two unknowns (E_z and χ), related through the contrast-source w. The integral approach methods all (try to) solve Equation (3.3) for the contrast-source w, and then reconstruct the field E_z from Equation (3.2), after which the contrast is easily solved from Equation (3.1).

For all global equation based reconstruction methods, the required fields for reconstruction are the $B_1^{\mathrm{sc};+}$ field and the background field E_z^b. The measured field is the total B_1^+, to derive the scattered field from this a measurement or simulation without contrast ($B_1^{\mathrm{b};+}$) can be carried out and subtracted

$$B_1^{\mathrm{sc};+} = B_1^+ - B_1^{\mathrm{b};+} \tag{3.4}$$

3.1.1. Iterative inversion

One method to iteratively reconstruct the contrast-source (and contrast) from a measured field is the CSI method [17]. This can be derived from the set of equations described in Section 3.1. Multiplying Equation (3.2) on both sides with χ, and combining it with Equation (3.1) yields the object or state equation as

$$w = \chi E_z^{\mathrm{b}} + \chi G_{\mathrm{D}}\{w\}, \quad \mathbf{x} \in \mathcal{D}. \tag{3.5}$$

Where $G_{\mathrm{D}}\{\cdot\}$ is essentially the operation of the Green's function (the calculation of the vector potential) on the operand (the contrast-source)

$$G_{\mathrm{D}}\{w\} \equiv k^2 \int_{\mathbf{x}' \in \mathcal{D}} G(\mathbf{x} - \mathbf{x}') w(\mathbf{x}', \omega)\, \mathrm{d}V. \tag{3.6}$$

The data equation 3.3 can be rewritten as

$$f(\mathbf{x}, \omega) = G_{\mathrm{S}}\{w(\mathbf{x}, \omega)\}, \quad \mathbf{x} \in \mathcal{S}. \tag{3.7}$$

Here $f \equiv B_1^{\mathrm{sc;+}}$ to follow literature conventions, and the operator is defined as

$$G_{\mathrm{S}}\{w\} \equiv -\frac{\mu_{\mathrm{b}} k_{\mathrm{b}}^2}{2\zeta_{\mathrm{b}}} \left(\partial_y + \mathrm{j}\partial_x\right) \int_{\mathbf{x}' \in \mathcal{S}} G(\mathbf{x} - \mathbf{x}') w(\mathbf{x}', \omega)\, \mathrm{d}V. \tag{3.8}$$

In the equations above, the subscript D and S on the operators are added to differentiate between the two operations and accentuate the location of the point $\mathbf{x}$. In the MRI scenario both the contrast domain ($\mathcal{D}$) and measurement domain ($\mathcal{S}$) are the same domain. This is different from most general inversion applications, where measurements are taken outside of the contrast domain.

Equation (3.5) and Equation (3.7) are the two equations from which the unknown contrast-source w, contrast χ and field E_z will be reconstructed. To solve this non-linear set of equations, the CSI method employs an alternating update direction gradient search algorithm. This iteratively first reconstructs a contrast-source, and then a contrast, which is repeated. This is done while minimising the cost function

$$F(w_j, \chi) = \frac{\|f - G_{\mathrm{S}}\{w_j\}\|_{\mathrm{S}}^2}{\|f\|_{\mathrm{S}}^2} + \frac{\|\chi E_z - w_j\|_{\mathrm{D}}^2}{\|\chi E_z^{\mathrm{b}}\|_{\mathrm{D}}^2}. \tag{3.9}$$

A more thorough description can be found in [16]. A definition of the norms can be found in Appendix A.

This method has been applied to MRI before [3] and will be used as a reference, notes on the specific implementation can be found in Chapter 4.

3.1.2. Single-step inversion

In the single-step inversion methods the goal is to solve Equation (3.3) for the contrast-source w in a single-step. After this the total field is reconstructed using w, and then the contrast is found from w and E_z. Solving Equation (3.3) for w is possible because the measured field (B_1^+) is measured in the same domain $\mathcal{D}$ as the contrast.

Solving the equation through deconvolution is first described, after which a more robust approach is described in which a minimum norm is considered. After this the necessary steps to go from contrast-source to contrast are outlined.

Operator

The Green's function that is used to relate the $B_1^{\mathrm{sc};+}$ field to the contrast-source, as it is mentioned in Equation (3.3) can be written as

$$G_{\mathrm{S}}\{w\} = \underbrace{\frac{-\mu_b}{2\zeta_b}\left(\partial_y + \mathrm{j}\partial_x\right)}_{\text{differentiation}} \cdot \underbrace{k_{\mathrm{b}}^2 \int_{\mathbf{x}'\in\mathcal{S}} G(\mathbf{x}-\mathbf{x}')w(\mathbf{x}')\,\mathrm{d}V}_{\text{Green's function}}. \tag{3.10}$$

Numerically this function can be implemented in two distinct ways. One is separated as above with the Green's function and the differentiation operator as separate functions. The other is to apply the differentiation analytically to the Green's function and then calculate that operator numerically. More information on this can be found in [5], and the derived operator can be found in Equation (4.4).

There are a number of advantages for the second approach. First, it requires the same size Green's operator as before, and the Green's function will be calculated as it would in the separated case. Now the end result needs one less matrix vector multiplication (which is needed for the differentiation operator). Therefore, it should be faster. Secondly, as the derivative is calculated analytically it does not introduce rounding errors, while a numerical application would. Lastly, finding the adjoint or inverse operation of this operator is much more straightforward. Therefore the 'nabla-Green' combined operator will be used in the single-step inversion methods.

The operator with the differentiation applied to the Green's function will be denoted with a ∇ superscript

$$G_{\mathrm{S}}^{\nabla}\{w\} = \frac{-\mu_b k_{\mathrm{b}}^2}{2\zeta_b} \int_{\mathbf{x}'\in\mathcal{S}} G^{\nabla}(\mathbf{x}-\mathbf{x}')w(\mathbf{x}')\,\mathrm{d}V. \tag{3.11}$$

Deconvolution

As described in [13], to invert the convolution operation of the G_{S}^{∇} operator, a deconvolution operation can be applied. To clarify, Equation (3.3) will be rewritten using spatial Fourier transforms to change the convolution into a multiplication

$$\mathcal{F}\{B_1^{\mathrm{sc};+}\} = -\frac{\mu_b k_{\mathrm{b}}^2}{2\zeta_b} \cdot \left(\mathcal{F}\{G^{\nabla}\} \cdot \mathcal{F}\{w\}\right). \tag{3.12}$$

Here $\mathcal{F}$ is used to denote the spatial Fourier transform. Now, to solve this equation for w in the Fourier domain, a division can be used

$$\mathcal{F}\{w\} = -\frac{2\zeta_b}{\mu_b k_{\mathrm{b}}^2} \frac{\mathcal{F}\{B_1^{\mathrm{sc};+}\}}{\mathcal{F}\{G^{\nabla}\}}, \tag{3.13}$$

and with the inverse Fourier transform applied, we find that

$$w = -\frac{2\zeta_b}{\mu_b k_{\mathrm{b}}^2} \cdot \mathcal{F}^{-1}\left\{\frac{\mathcal{F}\{B_1^{\mathrm{sc};+}\}}{\mathcal{F}\{G^{\nabla}\}}\right\} \tag{3.14}$$

is the solution. Unfortunately, numerically this approach is not very robust for three reasons. Firstly, the Fourier transform of the data $B_1^{\mathrm{sc};+}$ does not give a stable result as the data is only available in the imaging region, and therefore requires apodisation or windowing with a low-pass filter. This in turn reduces the accuracy of the inversion, as sharp contrasts are smoothed. Secondly, the 'nabla-Green's' operator is an odd operator at the points where the source point is equal to the measurement point, which results in a division by zero in above equation. This means that the Green's function needs to be artificially scaled at the origin (in

the angular wave domain) to compensate for this. Lastly, there is no regularisation possible against noise, although noise is not a big issue in this application due to the apodisation step that already filters noise (and information).

To improve on this using a more robust method, the minimal norm estimation is considered in the next section.

Minimum norm solution

Instead of deconvolving the Green's function with the measured field, another approach is to estimate a possible contrast-source, and then minimising the error between the estimate and the measured field. In this way no deconvolution has to be carried out. As the system is ill posed, an error norm is used to find an optimum solution. This minimum norm problem can be stated as

$$w = \min_{w_{\text{est}}} \|G_{\text{S}}\{w_{\text{est}}\} - B_1^{\text{sc;+}}\|_p. \tag{3.15}$$

Here w_{est} is the estimated contrast-source, and $\|\cdot\|_p$ is used to denote the p-norm. No pointwise division operation is required to circumvent the numerical problems that the deconvolution approach suffers from.

There is also flexibility in the choice of norm and solver. The choice of norm can influence the reconstruction.

Euclidian norm least-squares The first norm that is considered is the much used ℓ_2 norm. This turns the above problem into a least squares problem.

Much research has been done into solving least squares problems [4]. One direct advantage is that when using an iterative minimisation algorithm, the number of iterations can be used as a regularisation parameter. This can help to suppress noise, or make a tradeoff between reconstruction speed and accuracy. Another advantage is the wide range of preconditioners that have been researched for such problems. Using specific preconditioners for piecewise-constant media (as the MRI contrast is) could potentially speed up convergence and even improve accuracy. In the implementation of this method the LSQR algorithm has been used in Matlab®.

ℓ_1 norm least-squares Another norm that can be interesting given the piecewise-constant contrast is the ℓ_1 norm. However, a downside of the ℓ_1 norm is that it is more difficult to find the minimum (e.g. slower convergence). This also means that the algorithms are generally less stable. The ℓ_1 norm minimisation was implemented using iterative reweighed least squares (IRLS) [4]. A comparison of the different norms can be found in Appendix E. In the two-dimensional case they perform almost identical, but the computational complexity of the ℓ_1 norm is much higher (7 hours running the algorithm to get a comparable results to 5 minutes of the ℓ_2 solution) that it is deemed infeasible for further investigation at this time.

Huber norm A way to get the best of both ℓ_1 and ℓ_2 norms is using the Huber norm. This is a hybrid ℓ_1/ℓ_2 error measure. It uses a threshold to determine when to use the ℓ_1 or the ℓ_2 norm and can be tuned to perform like either one of them [9]. The goal is to tune it in a way that the ℓ_1 is used at discontinuous areas and the ℓ_2 norm to smooth out the constant areas.

Reconstruction

Once the contrast-source is found using one of the previously mentioned methods, the next step is to compute the contrast. To do this, first the electric field is calculated and then the least squares solution for the contrast.

The total electric field is the sum of the background or incident field and the scattered electric field due to the contrast. Explicitly, we have

$$E_z(\mathbf{x}) = E_z^{\mathrm{b}}(\mathbf{x}) + G_{\mathrm{D}}\{w(\mathbf{x}, \omega)\}. \tag{3.16}$$

If the background electrical field (E_z^{b}) of the MRI scanner is known (either simulated or measured), the equation can be computed for the total field E_z.

Simply dividing the contrast-source by the total field should give the contrast, as can be seen in Equation (3.1). However, the field can be very small (close to 0), which can result in some problems when this is done numerically. Therefore, the least squares solution for the contrast is used, which is given by

$$\chi = \frac{w\overline{E_z}}{E_z\overline{E_z}}, \tag{3.17}$$

where the overbar denotes a complex conjugate. It should be noted that the contrast χ will be equated to 0 when the total field E_z is 0. This concludes the single-step reconstruction methods.

3.2. Differential approach

The differential approaches are derived from the local form of Maxwell's equations, 2.7 and 2.8. First the Helmholtz equation and corresponding inversion technique is described, which is widely used in EPT and relies on the assumption that the medium is homogeneous. After this a new method is proposed that works because the measurement and source domain are equal in an MRI setting. Therefore, the inversion problem can almost be reworked into a forward problem and solved analytically.

3.2.1. Naive EPT based on Helmholtz's equation

To arrive at the Helmholtz equation the following assumptions have to be made:

1. There are no external currents inside the human body;
2. The contrast is homogeneous;

Rewriting Maxwell's equations with these assumptions gives

$$-\nabla \times \mathbf{H} + \eta \mathbf{E} = 0, \tag{3.18}$$

$$\nabla \times \mathbf{E} + \zeta \mathbf{H} = 0. \tag{3.19}$$

Now, taking the divergence of Equation (3.19) gives

$$\nabla \cdot \nabla \times \mathbf{E} + \zeta \nabla \cdot \mathbf{H} = 0,$$

and since the divergence of a curl is always zero ($\nabla \cdot \nabla \times \mathbf{E} = 0$), we find

$$\zeta \nabla \cdot \mathbf{H} = 0, \tag{3.20}$$

which shows that $\mathbf{H}$ is divergence free. Using the same procedure as before when deriving the homogeneous solution, but this time substituting $\mathbf{E}$ in Equation (3.19) instead of $\mathbf{H}$, ($\mathbf{E} = 1/\eta \nabla \times \mathbf{H}$) in the first leads to

$$\frac{1}{\eta} \nabla \times (\nabla \times \mathbf{H}) + \zeta \mathbf{H} = 0. \tag{3.21}$$

Using a vector identity and the fact that $\mathbf{H}$ is divergence free yields

$$\nabla \times (\nabla \times \mathbf{H}) = \nabla(\nabla \cdot \mathbf{H}) - \nabla^2 \mathbf{H} = -\nabla^2 \mathbf{H}. \tag{3.22}$$

Putting this back into Equation (3.21) gives

$$-\frac{1}{\eta}\nabla^2 \mathbf{H} + \zeta \mathbf{H} = 0. \tag{3.23}$$

Substituting $\mathbf{B}$ into the equation (through the constitutive relations) and multiplying both sides by $-\frac{\mu\eta\zeta}{\zeta} = \frac{\mu k^2}{\zeta}$ leads to the Helmholtz equation

$$\nabla^2 \mathbf{B} + k^2 \mathbf{B} = 0, \tag{3.24}$$

where $k^2 = \mu\varepsilon\omega^2 - \mathrm{j}\mu\sigma\omega$ relates to the electrical properties of the object.

The Helmholtz equation is valid for all Cartesian components, so to solve this equation using the B_1^+ field it can be rewritten as

$$\frac{\nabla^2 B_1^+}{B_1^+} = -k^2. \tag{3.25}$$

This leads to the conductivity and permittivity to be reconstructed as

$$\varepsilon = -\Re\left\{\frac{\nabla^2 B_1^+}{B_1^+}\right\}\frac{1}{\mu\omega^2}, \quad \text{and} \quad \sigma = \Im\left\{\frac{\nabla^2 B_1^+}{B_1^+}\right\}\frac{1}{\mu\omega}, \tag{3.26}$$

The homogeneous assumption unfortunately does not hold in the human body [20]. Another issue with this method is the Laplacian (the ∇^2 term). Using a second order derivative makes the method very susceptible to noise.

3.2.2. First-order-differentiation inversion

The total magnetic field $\mathbf{H}$ is related to the $\mathbf{E}$ field through Maxwell's equations. This relation can be used, in absence of external sources (which is true inside the body), to directly relate the two variables through spatial derivatives. This can lead to a reconstruction operation as follows. Defining the operator

$$P \equiv \frac{-2c_0^2}{\mathrm{j}\omega\mu_0}(\partial_y + \mathrm{j}\partial_x), \tag{3.27}$$

with $c_0 = 1/\sqrt{\varepsilon_0\mu_0}$, and applying it to the total B_1^+ field yields

$$PB_1^+ = (\chi + 1)E_z. \tag{3.28}$$

Furthermore, the integral equation for E_z is

$$E_z - \int_{\mathcal{D}^{\mathrm{sc}}} G\chi E_z \,\mathrm{d}V = E_z^{\mathrm{b}}. \tag{3.29}$$

Subtracting $\int_{\mathcal{D}^{\mathrm{sc}}} GE_z \,\mathrm{d}V$ inside, and adding it outside of the integral on the left-hand side (which is possible due to linearity of the operator) gives

$$\begin{aligned} E_z + \int_{\mathcal{D}^{\mathrm{sc}}} GE_z \,\mathrm{d}V - \int_{\mathcal{D}^{\mathrm{sc}}} G(\chi+1)E_z \,\mathrm{d}V &= E_z^{\mathrm{b}}, \\ E_z + \int_{\mathcal{D}^{\mathrm{sc}}} GE_z \,\mathrm{d}V - \int_{\mathcal{D}^{\mathrm{sc}}} GPB_1^+ \,\mathrm{d}V &= E_z^{\mathrm{b}}, \\ E_z + \int_{\mathcal{D}^{\mathrm{sc}}} GE_z \,\mathrm{d}V &= \underbrace{E_z^{\mathrm{b}} + \int_{\mathcal{D}^{\mathrm{sc}}} GPB_1^+ \,\mathrm{d}V}_{\text{known}}. \end{aligned} \tag{3.30}$$

This is the standard scattering integral equation with homogeneous contrast equal to -1, which can be solved numerically for E_z. The contrast then follows from

$$\chi = \frac{PB_1^+ \overline{E}_z}{|E_z|^2} - 1. \tag{3.31}$$

The advantage of this approach is that there are no assumptions of homogeneity made on the contrast. Also, this method only features a single spatial derivative instead of a second order derivative as the Helmholtz approach requires. Even though the differentiation part is only first order, the method overall is a little more complex than the Helmholtz due to Equation (3.30) that needs to be solved iteratively. Fortunately that equation is very well-behaved, and generally converges to a normalised 2-norm residual of less than 10^{-6} within 5 iterations.

3.3. Summary

To summarise, two new methods have been proposed, and one method will be reviewed:

- the direct contrast source EPT method;
- the first order differentiation method;
- the CSI method will be reviewed.

The reconstructions made with these will be compared with

- the original contrast;
- the Helmholtz based reconstruction;
- the deconvolution based reconstruction.

The results of this will be shown in Chapter 5. The CSI method will also be reviewed and the algorithm slightly altered.

4

Data sets and the implementation of the EPT operators

In this chapter the used datasets and the implementation of previously described methods in Matlab® are elaborated. For these methods the main operators and their equations are repeated as well as a numerical implementation of them is given. This is done to aid in reproducing the results obtained in this thesis.

Four different datasets have been used to test the algorithms described in the previous chapter. In particular, we have considered

1. A 2D simulated pelvis slice.
2. A 3D simulated shoulder slice.
3. An in vivo measurement of the head.
4. Three Phantom measurements.

First the simulated datasets and the original contrast used for these are discussed, after that the in vivo and phantom dataset is discussed. An overview of all the datasets can be found in Table 4.1.

4.1. Simulated datasets

For the 2D dataset, the female Ella body model of the ITIS foundation [6] is used, while for the 3D dataset the male Duke model is used. These have an isotropic voxel size of $2.5\mathrm{mm}$ in the two-dimensional case, and $5\mathrm{mm}$ in the three-dimensional case.

The forward simulation in the two-dimensional case has been performed in Matlab®. Here 16 line sources have been placed (equally spaced) on a circle around the pelvis slice at a radius of $0.34\mathrm{m}$. These line sources have been excited using a quadrature phase field at $128\mathrm{MHz}$ ($3\mathrm{T}$) and their influences are summed to arrive at the final background field.

The forward simulation in the 3D case has been performed in Remcom[1]. Here a birdcage body coil (diameter coil $610\mathrm{mm}$, diameter shield $680\mathrm{mm}$, length coil $560\mathrm{mm}$) is fed using a $128\mathrm{MHz}$ ($3\mathrm{T}$) RF signal to generate the background field.

[1] Remcom XFdtd software, v.7.5.0.3, State College, PA, USA.

Source	Resolution	Domain	Scanner used	r (m)
Ella	2.5 mm	2D	line sources	0.34
Duke	5 mm	3D	Birdcage	0.305
In-vivo	5 mm	3D	Birdcage	0.35
Phantom	5 mm	3D	Birdcage	0.35

Table 4.1: Overview of used datasets.

Type	Name	Short form
Contrast source	Contrast source inversion	CSI
Single-step	Deconvolution inversion	Decon.
	Minimum norm inversion	MinNorm.
Differentiation	Naive EPT based on Helmholtz	Helmholtz
	First-order-differentiation inversion	Diff.

Table 4.2: Overview of used methods and nomenclature.

4.2. Real dataset

The in vivo and phantom measurements were performed at the University of Utrecht medical center. The in vivo measurements have been measured using an Ingenia $3\mathrm{T}$ MRI scanner.[2] The phantom datasets have been measured on an older Achieva $3\mathrm{T}$ MRI scanner. For these measurements three different phantoms have been placed into the scanner, with conductivities ranging from no conductivity to eight and sixteen siemens per meter.

4.3. Computational implementation

In this section the implementation of the algorithm and the discretisation of various operators and functions is discussed. First the single step inversion methods, and after that the finite differencing methods are discussed. The CSI method is implemented as it is described in [3] with help of the original author.

To reiterate the methods as they are used and described in this thesis are found in Table 4.2.

4.3.1. Single-step

In the single step methods (both deconvolving and finding the minimum norm solution) the 'nabla-Green's' function

$$G_{\mathrm{S}}^{\nabla}\{w\} = \frac{-\mu_b k_{\mathrm{b}}^2}{2\zeta_b} \int_{\mathbf{x}' \in \mathcal{S}} G^{\nabla}(\mathbf{x} - \mathbf{x}') w(\mathbf{x}') \,\mathrm{d}V. \tag{4.1}$$

is used. The 'nabla-Green's' operator $G^{\nabla}(\mathbf{x} - \mathbf{x}')$ is in this function applied to a (source) field through a convolution. To implement this numerically, fast Fourier transforms (FFTs) have been implemented. In this way, the convolution is performed as a multiplication in the (spatial) Fourier domain.

This is a very powerful and fast way to calculate the convolutions. In Matlab® the computation has been implemented with the Green's operator already in the Fourier domain, so that the transform does not need to be computed every time. Zero padding is applied to the source

[2] For more information on the particulars of the measurement please contact the author of this thesis.

data to ensure that the periodicity requirement is fulfilled [22]. The source is zero padded to the next largest power of two, which should be equal to the Green's operator dimensions. The resulting function can be found in Listing 4.1.

Listing 4.1: Green's function

```
function field = greensFun(operator, source)
    % compute dimensions
    dim = size(source); fftDim = size(operator);
    % pad input for FFT
    source = padarray(source, fftDim-dim, 'post');
    % perform discrete convolution using FFT
    field = ifft2(operator .* fft2(source));
    % reshape output
    field = field(1:dim(1),1:dim(2));
end
```

Before the 'nabla-Green's' operator can be applied, it needs to be computed numerically. This is not straightforward, as the operator has a logarithmic singularity in 2D.

Weak-Green's To use the Green's operator in 2D (and 3D) it needs to be weakened because of its logarithmic singularity. Starting with Equation (2.40), and following the derivation presented in [12] yields the following equations for $\mathbf{x}$ outside of the singularity (non self patch elements, $\mathbf{x} \neq \mathbf{x}_\mathrm{s}$)

$$G^w(\mathbf{x}-\mathbf{x}_\mathrm{s}) = -\frac{\mathrm{j}}{2k_\mathrm{b}a} J_1(k_\mathrm{b}a) H_0^{(2)}(k_\mathrm{b}|\mathbf{x}-\mathbf{x}_\mathrm{s}|), \tag{4.2}$$

and inside the (previously) singular region (self patch elements)

$$G^w(\mathbf{0}) = -\frac{\mathrm{j}}{2k_\mathrm{b}a}\left[H_1^{(2)}(k_\mathrm{b}a) - \frac{2j}{\pi k_\mathrm{b}a}\right]. \tag{4.3}$$

Here k_b is the wavenumber, a the radius of the circular disk used to circumvent the singularity, J_1 is a Bessel function of the first kind, $H_0^{(2)}$ and $H_1^{(2)}$ are Hankel functions of the second kind (denoted by the superscript), and of zero and first order (denoted by the subscripts), and $\mathbf{x}$ the grid points the Green's operator is defined on.

Nabla-Green's The application of the differential operator on the Green's function gives the nabla-Green's function. The differential operator can be taken under the integral because the Green's operator in the (convolution) integral is well behaved.

The gradient of the (weak) Green's operator can then be found as

$$G^\nabla(\mathbf{x}-\mathbf{x}_\mathrm{s}) = \frac{\mathrm{j}}{2a} J_1(k_\mathrm{b}a) H_1^{(2)}(k_\mathrm{b}|\mathbf{x}-\mathbf{x}_\mathrm{s}|) \frac{\mathbf{x}-\mathbf{x}_\mathrm{s}}{|\mathbf{x}-\mathbf{x}_\mathrm{s}|} \tag{4.4}$$

using elementary differential rules and the Hankel derivative relation

$$\frac{\mathrm{d}}{\mathrm{d}z} H_n^{(2)}(z) = \frac{n}{z} H_n^{(2)}(z) - H_{n+1}^{(2)}(z). \tag{4.5}$$

Furthermore, due to the multiplication with $\mathbf{x}-\mathbf{x}_\mathrm{s}$ the previously singular region (point) becomes zero, $G^\nabla(\mathbf{0}) = 0$.

The discretised matrix form of the operators can be found in Appendix D. To generate the numerical form of these is straightforward with a coordinate mesh generated with meshgrid and then using the besselj and besselh commands for the Bessel and Hankel functions.

4.3.2. Differentiation operators

Both when separating the Green's function from Equation (3.10), and in the differentiation used in the first order differentiation method defined in Equation (3.27), reproduced here for convenience

$$G_{\mathrm{S}}\{w\} = \frac{-\mu_b}{2\zeta_b}\left(\partial_y + \mathrm{j}\partial_x\right) \cdot k_{\mathrm{b}}^2 \int_{\mathbf{x}' \in \mathcal{S}} G(\mathbf{x} - \mathbf{x}')w(\mathbf{x}')\,\mathrm{d}V, \tag{4.6}$$

$$P \equiv \frac{-2c_0^2}{\mathrm{j}\omega\mu_0}(\partial_y + \mathrm{j}\partial_x). \tag{4.7}$$

A differencing operator is used. In both cases this operator looks like

$$D = \partial_y + \mathrm{j}\partial_x. \tag{4.8}$$

To discretise this operation, a central differencing scheme is used for the partial differential operations. For example the derivative $\partial_x A_z|_{\mathbf{x}=\mathbf{x}_{m,n}}$ (at point m, n) is approximated as

$$\partial_x A_z|_{\mathbf{x}=\mathbf{x}_{m,n}} \approx \frac{A_z(\mathbf{x}_{m+1,n}) - A_z(\mathbf{x}_{m-1,n})}{2\delta x} \tag{4.9}$$

The discretisation of this operation can be found in Appendix D.

4.3.3. Simulated additive noise considerations

A well done measurement ranges in signal to noise ration (SNR) from 90 to 120 dB.[3] Often publications of simulated methods that add noise artificially to their measurements will go down to as far as 30 dB SNR, but this turns out not to be necessary at all.

Another thing often neglected is that the phase noise and amplitude noise are generally from two different measurements, hence the noise should be added separately, with their respectively different SNR levels. The SNR of the amplitude measurement is expected to be lower as this measurement is more difficult to do than the phase only measurement.

[3] Based on experiences from MRI technicians on in-situ measurements of human volunteers.

5

Reconstruction results

In this chapter the simulation and reconstruction results are presented. The different methods used are:

1. Contrast source inversion: Iterative method employing an alternating update direction gradient search algorithm to solve for a contrast source parameter and the contrast.
2. Deconvolution: Direct method deconvolving the measured field with the Green's function to reconstruct the contrast source, and from it the contrast.
3. Direct contrast source EPT: Iterative method finding through a minimum norm the 'best fit' contrast source, and from it the contrast.
4. First order differentiation: Direct method which reconstructs a contrast through the relation provided by the differential form Maxwell's equations.
5. Helmholtz based: Direct method which reconstructs the contrast through Maxwell's equations assuming a homogeneous contrast.

First the contrast sources that are reconstructed using the contrast source (CS) type methods are compared to the originals. After this the general reconstructions are shown. Lastly, some additional profiles have been constructed to more clearly compare the different methods. These comparisons are presented at the end of each section.

The phantom datasets have a number of complications, which lead to ambiguous results. Therefore it was chosen to discuss these in Appendix F separate from the main results discussed in this thesis.

5.1. Diagonalised CSI

While implementing the CSI method as proposed by Balidemaj et al. [3] a diagonalised CSI scheme [1] was investigated. In this scheme the update procedure for the contrast is foregone, and instead a regularisation parameter is introduced.

It turns out that this produces essentially the same results as the CSI method. This could be because the data error in regular CSI is much smaller than the contrast source error. This is because both the field and the contrast are estimated and compared to the contrast source. Since the contrast source is also the input parameter to estimate the field and contrast these should not introduce an error.

This small data error leads to a small influence of the contrast reconstruction part on the total reconstruction. This explains why a simple regularisation constant leads to the same

# iter	F_{regular}	F_{diagonal}	$t_{\text{regular}}(s)$	$t_{\text{diagonal}}(s)$
10	2.331e-2	2.331e-2	0.6428	0.4600
100	3.106e-4	3.106e-4	5.7384	4.3277
500	9.948e-5	9.948e-5	13.542	10.273

Table 5.1: Results for the cost function and algorithm time between diagonalised CSI and regular CSI.

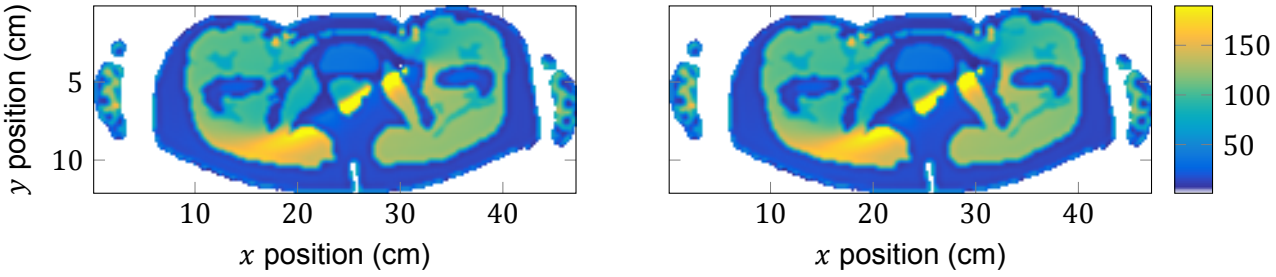

(a) Original CSI reconstruction

(b) diagonal CSI reconstruction

Figure 5.1: Absolute value of reconstructed contrasts using the direct method for the 2D simulation with additive gaussian noise at SNR = 30dB.

results. An advantage of the diagonalised scheme is that it is about 20% faster due to a number of calculations that do not have to be performed (for reconstructing the field and contrast). The contrast can then still be reconstructed from the end result for the contrast source, but this is a single step as opposed to performing the calculation every iteration.

Cost function and running time results of the diagonalised CSI and regular CSI method can be found in Table 5.1, and a figure of the reconstruction results can be found in Figure 5.1. Based on these results, the diagonalised approach is used in this thesis whenever the CSI method is mentioned.

5.2. Two-dimensional reconstructions

The 2D forward simulation is done using the same equations as described in Chapter 3. In this simulation the most notable simplification is the fact that it is modeled using perfect two-dimensional E-polarised fields. This is the reason that the slice used here is a pelvis slice (since in this region the assumptions generally hold). This also means a simple transmitter array of 16 line sources can be used.

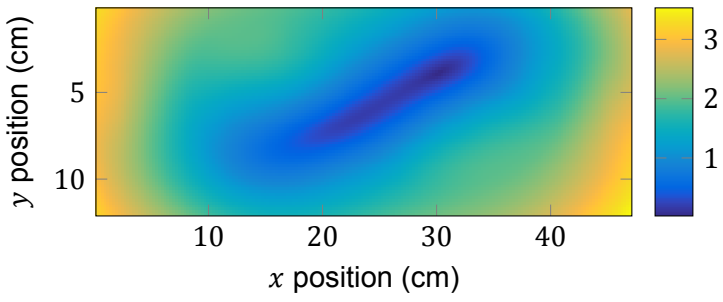

Figure 5.2: Total E field of the 2D simulation, $\mathrm{V} \cdot \mathrm{m}^{-1}$.

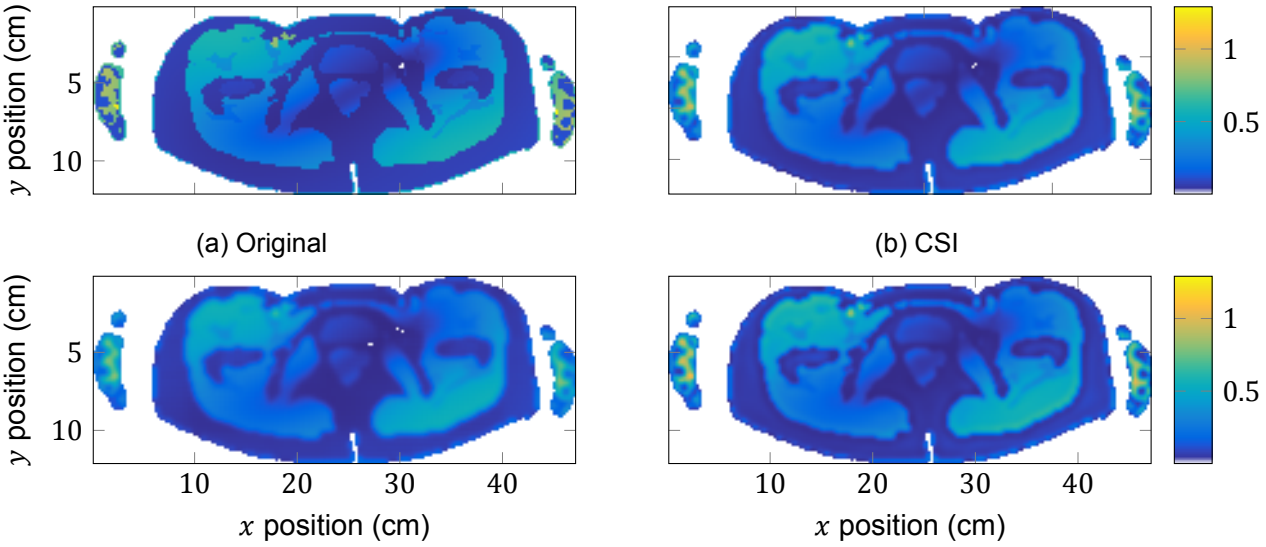

Figure 5.3: Absolute value of original and reconstructed contrast sources for the 2D simulation. The colorbar is scaled by 10^{-5} (the range is originally $[0, 1.2 \cdot 10^{5}]$).

5.2.1. Contrast-source

The contrast source reconstructions can be found in Figure 5.3. In this figure it can be clearly seen that the deconvolution reconstruction is smoothed out more than the other reconstructions, but all three resemble the original contrast source accurately. The dark 'spot' in the middle of the contrast sources is related to the dip in the electric field, which is shown in Figure 5.2. The normalised 2-norm of the error of these reconstructions can be found in Table 5.2.

5.2.2. Contrast

Three different contrast reconstructions have been computed using the above mentioned inversion methods, the absolute value, the permittivity and conductivity. These can be found in that order in Figures 5.4 and 5.5.

To compare the overall reconstruction results, the absolute value gives a good indication. The smoothing effect in the deconvolution approach can be observed when compared to the CSI and direct reconstructions. In all of the CSI based reconstructions a smear across the center can be observed. This is due to the overall field strength. In the center of the contrast the magnitude of the electric field strength is low. This means that for the reconstruction there is less 'information' available, which leads to a reconstruction error. This error can be minimised through, for example, regularisation such as total variation regularisation (TV regularisation) as can be applied to the CSI method, or shimming with different field polarisations, or by using dielectric pads to shape the field at certain areas.

The small difference between the direct and the original CSI method can be attributed to the number of iterations taken (in both the LSQR algorithm used for the least squares solution in the robust method as well as the CSI iterations).

The differencing based methods show a much more homogeneous contrast (where the contrast is homogeneous), which is also where the assumptions for the Helmholtz method hold. However, the Helmholtz method actually has very large 'transients' at the boundaries of the piecewise constant medium. The first order differentiation method does not show these interestingly enough, but does show a dependence on the electric field, as a slight increase in contrast can be observed in the areas of lower field in the center of the reconstruction. In the

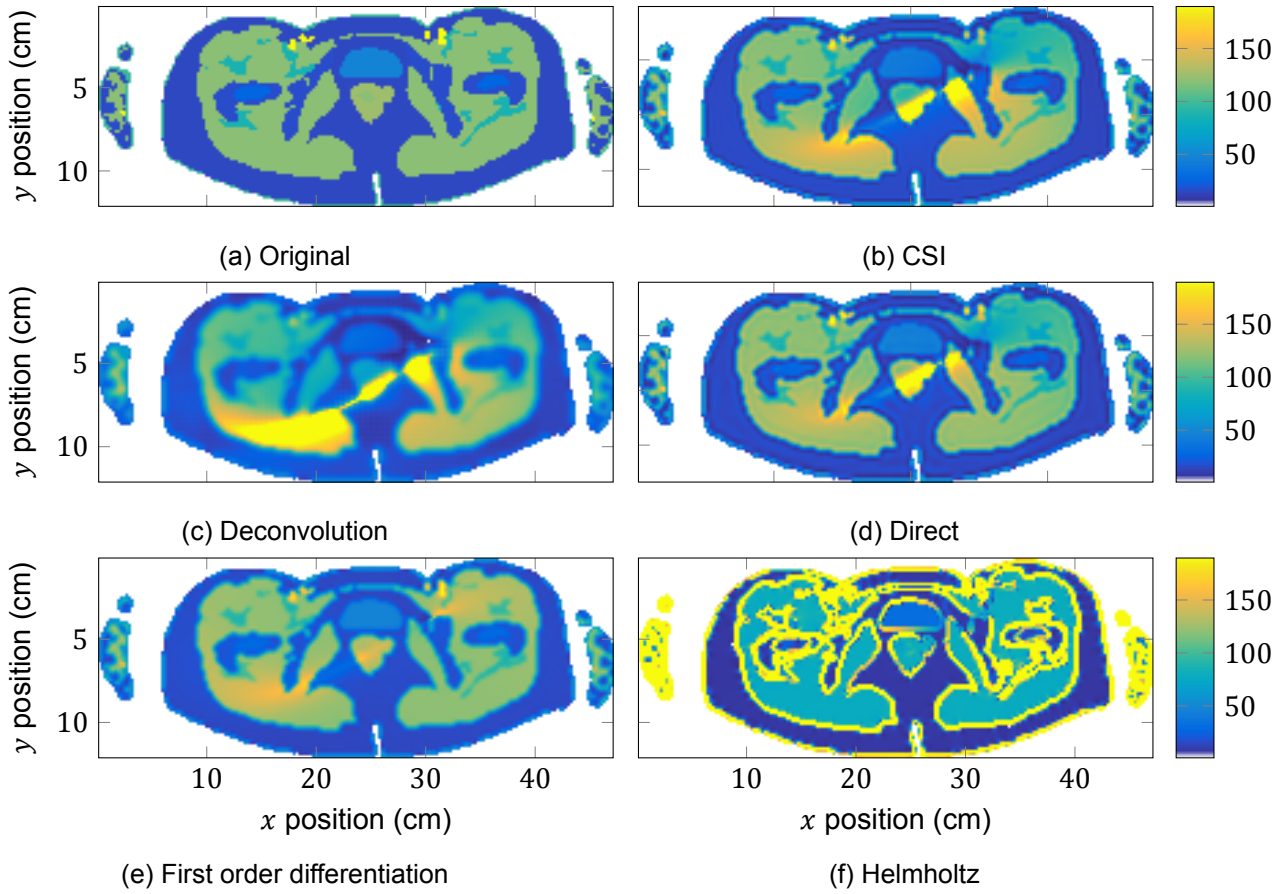

Figure 5.4: Absolute value of original and reconstructed contrasts for the 2D simulation.

permittivity and conductivity images the same observations can be made.

Noise

To compare the robustness to noise of the different methods, additive white gaussian (complex) noise was added to the data at an SNR of 50 (dB) based on the magnitude of the measured field, why this is done is explained in the next section.

From these images, found in Figure 5.6 it can clearly be seen that the Helmholtz method has the greatest problem with noise. Interesting to note is that the first order differentiation method does not have a big problem with noise although it also relies on differencing operators.

Reconstruction in the center of the other image has the most notable noise pattern, further indicating the reconstruction difficulty in this region.

Method	CS Error (normalised)	Contrast Error (normalised)
CSI	0.087	0.328
Direct	0.134	0.258
Deconvolution	0.156	0.565
Single diff.	N.A.	0.111
Helmholtz	N.A.	2.278

Table 5.2: Normalised 2-norm of error of contrast source (CS), and contrast ($\frac{\|x-\hat{x}\|_2}{\|x\|_2}$), where x is the original and $\hat{x}$ the reconstructed variable (χ or w).

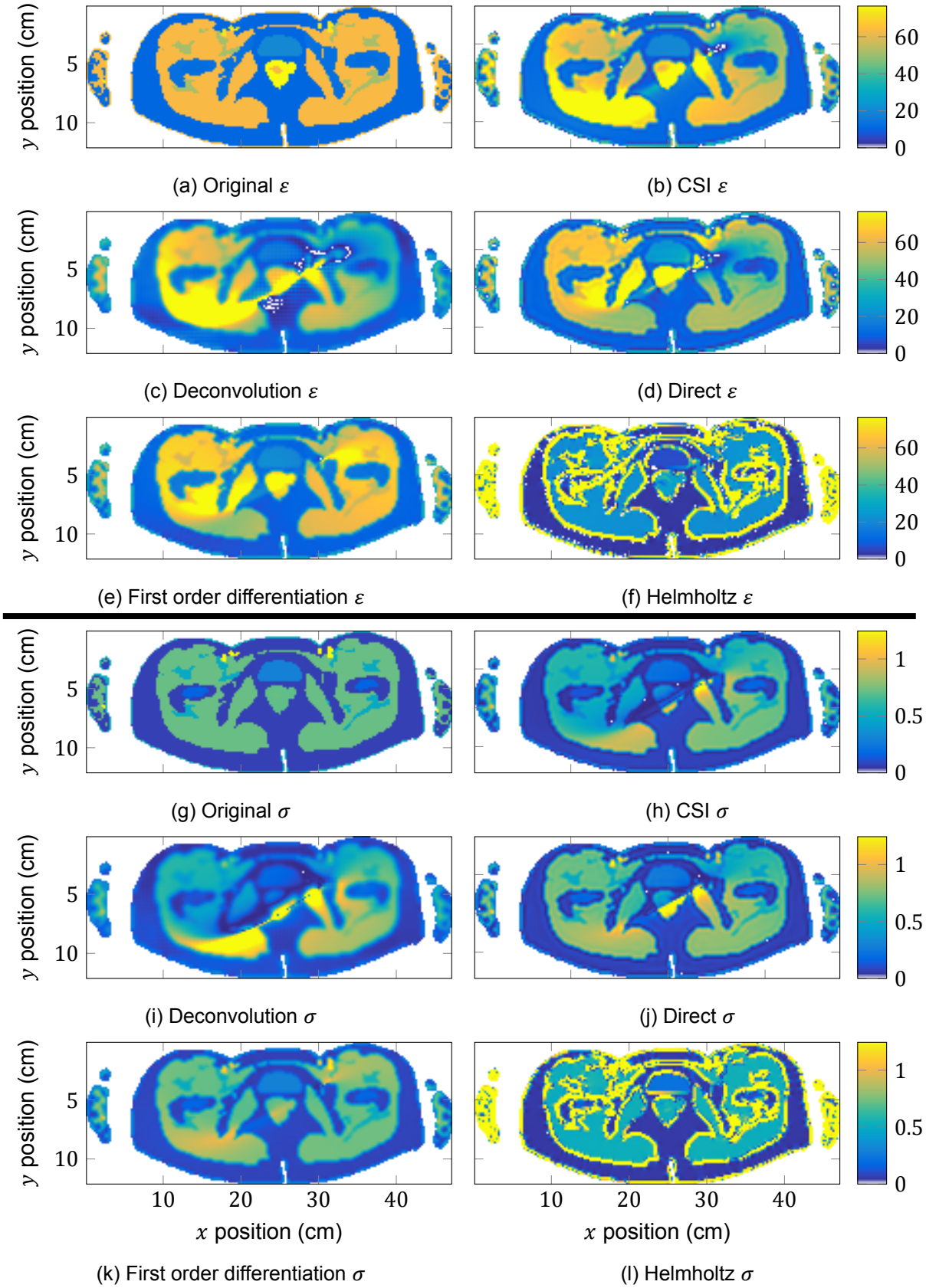

Figure 5.5: Permittivity ε and conductivity σ values of original and reconstructed contrasts for the 2D simulation. The original permittivity and conductivity can be found in Figures 5.5a and 5.5g. The reconstruction obtained using CSI in Figures 5.5b and 5.5h, those using the deconvolution approach in Figures 5.5c and 5.5i, those using the direct method in Figures 5.5d and 5.5j, those using first order differentiation approach in Figures 5.5e and 5.5k, and those using the Helmholtz based method Figures 5.5f and 5.5l.

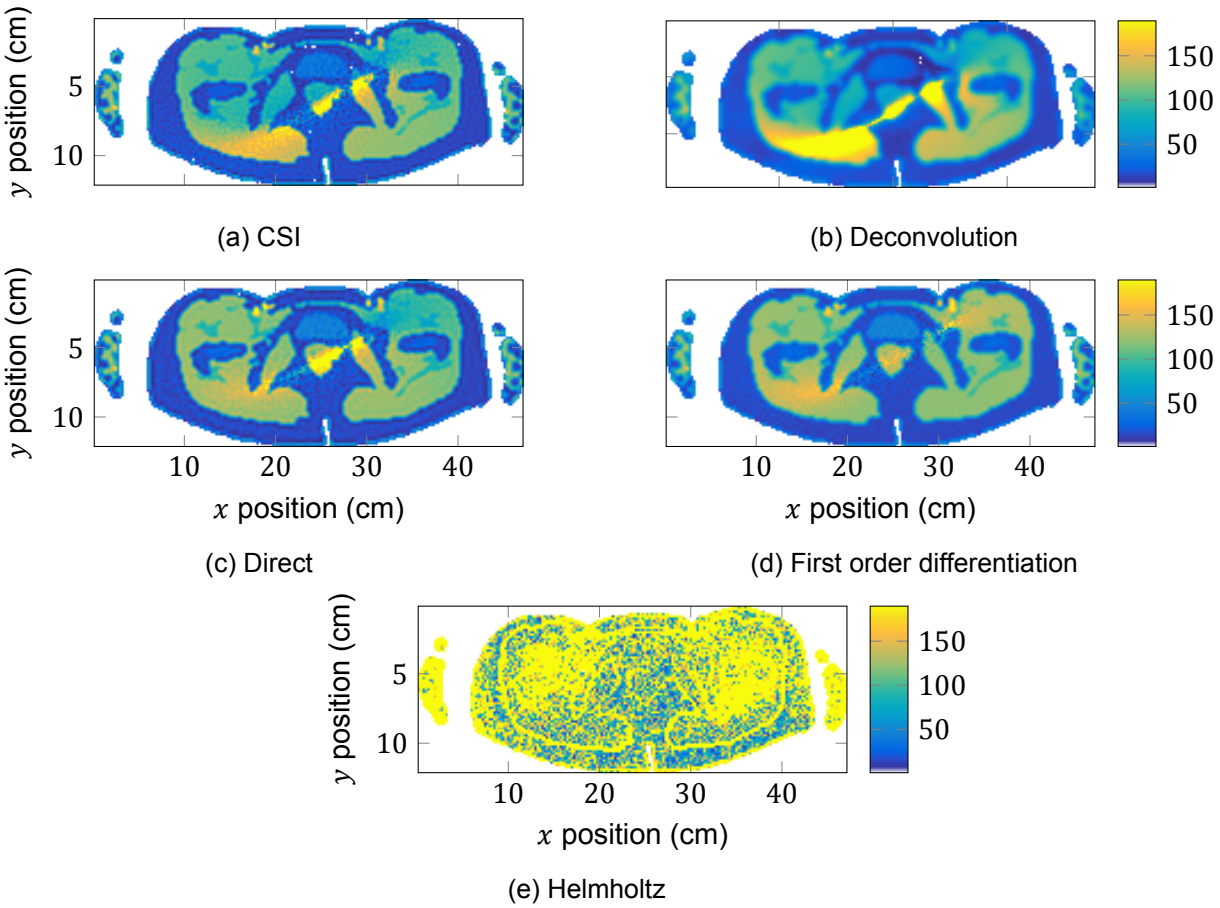

Figure 5.6: Absolute value of reconstructed contrasts for the 2D simulation with additive gaussian noise at SNR = 50dB.

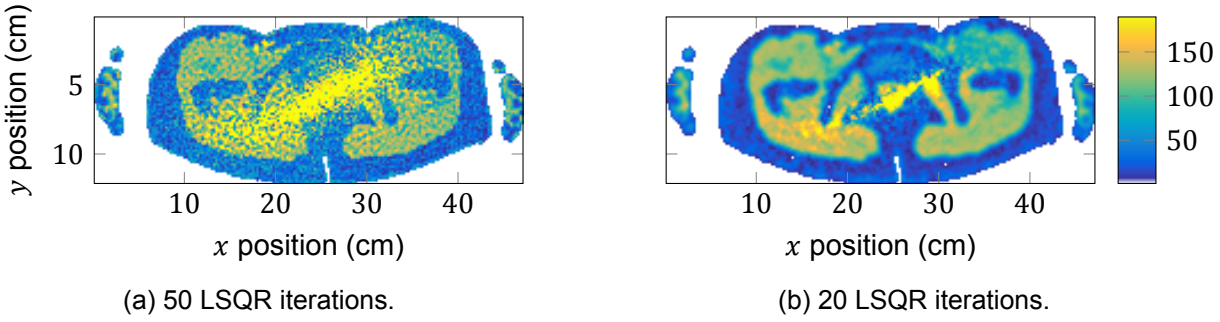

Figure 5.7: Absolute value of reconstructed contrasts using the direct method for the 2D simulation with additive gaussian noise at SNR = 30dB.

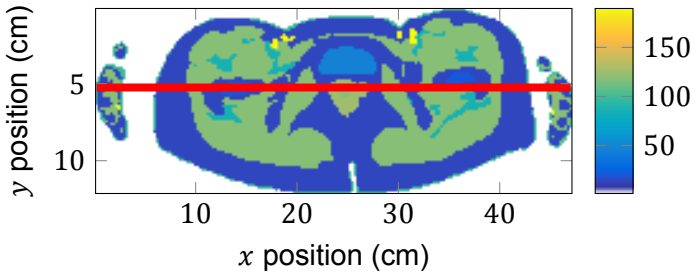

Figure 5.8: Absolute value of original contrast of 2D slice. Red line indicates location of cut-out.

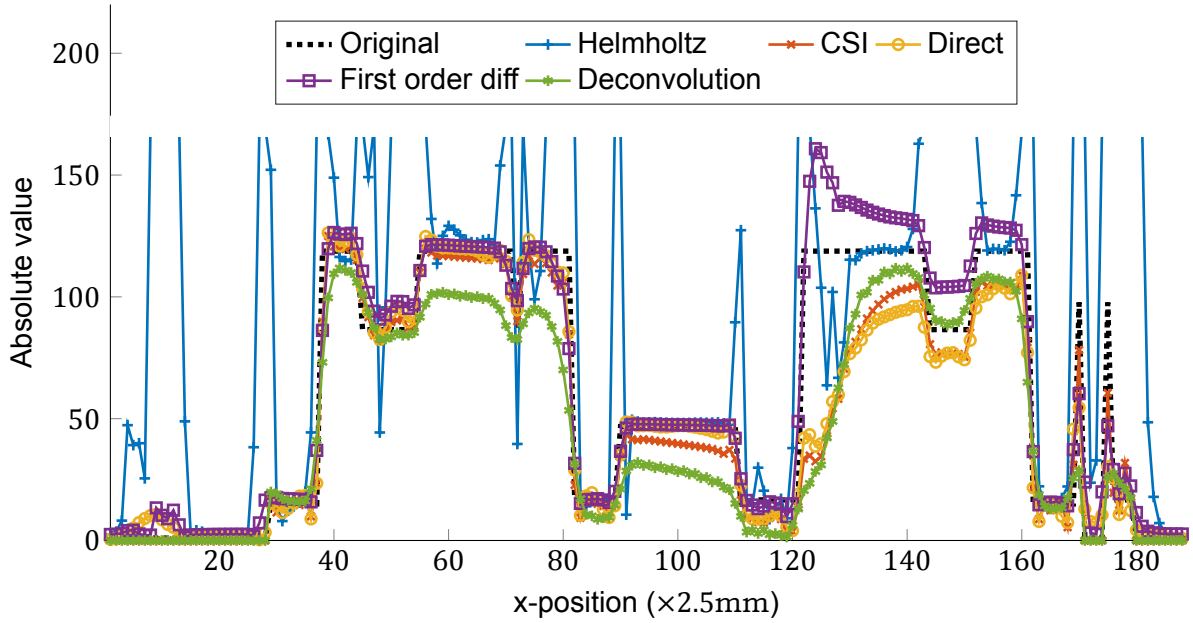

Figure 5.9: Absolute value of reconstructed and original contrast at location of cut out as indicated in Figure 5.8. The Helmholtz reconstruction has been truncated at 170 to declutter the graph.

Lastly, the deconvolution method does not display any noise influence. This has to do with the apodisation which acts as a noise filter. This 'effect' can be seen as well when using regularisation against noise, for example in the direct method as shown in Figure 5.7. In this figure the number of LSQR iterations is used as a regularisation parameter. In [3] it has been demonstrated that TV regularisation is also a very useful technique for noise regularisation.

Phase noise and amplitude noise As stated before, in a real MRI scanner the phase and amplitude of the B_1^+ field are measured in two separate measurements. This means that the noise component of these two will be different. The figures here have been made with complex noise based on the signal power, so not separate amplitude and phase noise. There are two reasons for this. First, the SNR is chosen at 50 dB, which is worse than real measurements would have, since at this level the effect of noise is visible on all reconstructions, and the large difference between the Helmholtz and other methods becomes clear. Second, a signal power based noise is chosen due to the fact that both amplitude and phase noise show the same type of effect. The only difference is that phase noise seems to have a larger impact on the reconstruction at an equal SNR than amplitude noise (if they are considered separately).

This is probably due to the fact that the phase is a variable modulo 2π, and not absolute, which means that for example phase measured at an SNR of 0 dB (phase and noise 'power' are equal) cannot provide distinguishable information anymore.

Reconstructions on a line

To give a more in depth view of the actual quality and accuracy of the reconstructions, we focus on reconstructions obtained along a line through the two-dimensional contrast profile as illustrated in Figure 5.8. The values of the reconstruction at this profile can be seen in Figure 5.9.

The Helmholtz reconstruction has been truncated at a magnitude of 170 to declutter the graph. It has also been scaled so that the homogeneous parts of the contrast line up with the actual values (this is not necessarily the case) but makes comparison easier between the methods.

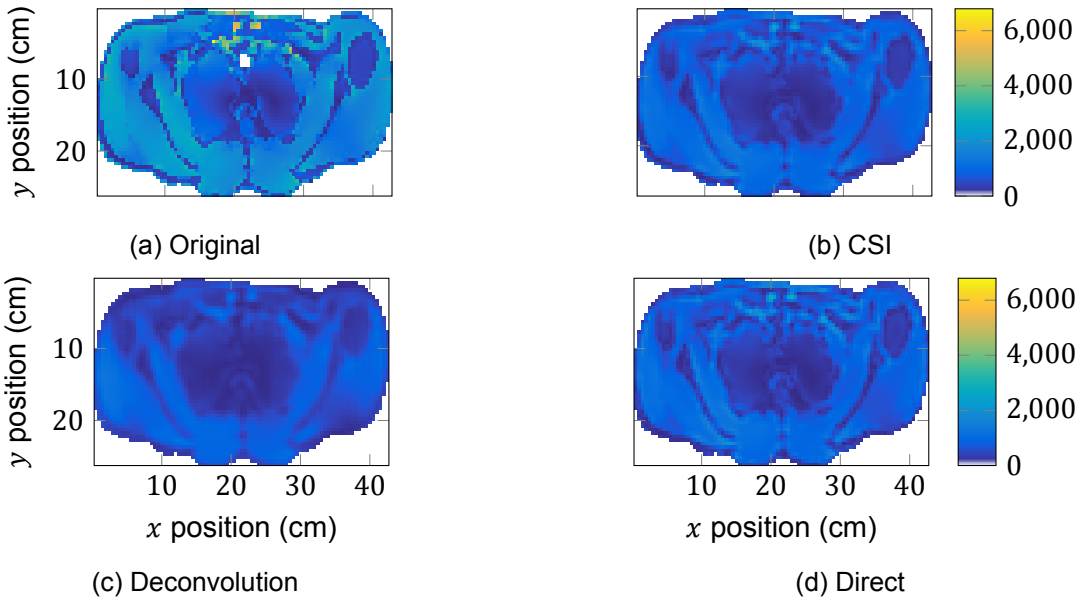

Figure 5.10: Absolute value of original and reconstructed contrast sources for the 3D simulation.

From the profile it can be clearly seen that the Helmholtz method largely overestimates the value of the contrast at the interfaces between two areas of different contrast. This is of course because especially there the assumption of a homogeneous contrast does not hold.

The deconvolution method tends to underestimate the contrast by a bit and has the smoothest transitions due to apodization, where a lot of high frequency information and some signal power is lost.

Another interesting observation is that at the left side the reconstruction is much better than at the right side. This is related to the strength of the electric field, which is low on the diagonal of the image as was already displayed in Figure 5.2. Therefore the right side of the reconstruction is more difficult, which is also shown in the graphical reconstruction in Figure 5.4. Interesting is that the first order differentiation method seems to overestimate the contrast where the CS based methods seem to underestimate the contrast. After about position 160 however, where the total field is stronger, these methods all again converge to the correct contrast.

5.3. Three-dimensional reconstructions

Even though the operators used are two-dimensional we can apply them to three-dimensional data. Obviously this introduces some complications. In comparison to the 2D reconstructions, the 3D case has a number of disadvantages, which explain the lower quality of reconstruction. Firstly, the slice taken is at the shoulders, so not in the middle of the scanner. This means that the background field is less homogeneous, as it is further from the centre of the MRI scanner.

Furthermore, the data is simulated in a three-dimensional forward simulation, which only further emphasises the problems when applying a 2D based reconstruction. This in combination with the less homogeneous background field deteriorates the assumption of a fully E-polarised field inside the contrast. One reason for this is that tissue in other parts of the body can (and will) scatter ‘into the slice under consideration with a field of which the polarisation is shifted, introducing field components that are not taken into consideration in the reconstruction.

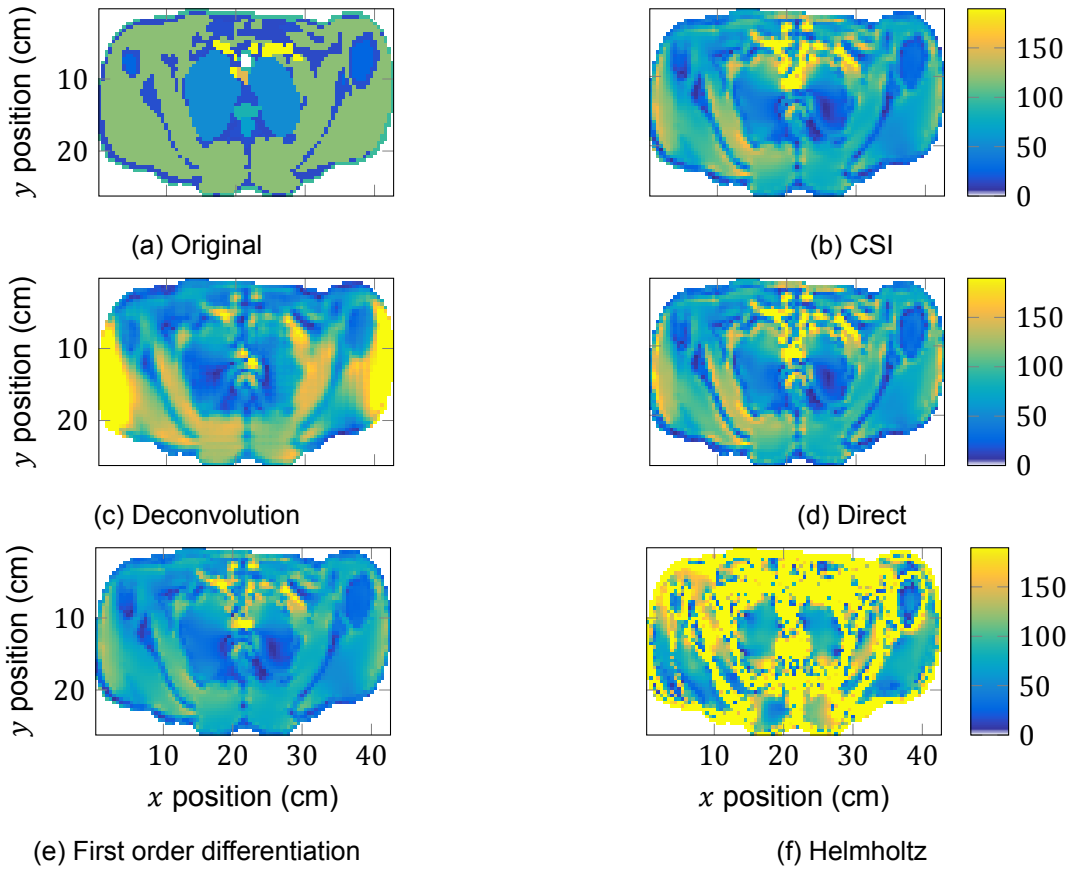

Figure 5.11: Absolute value of original and reconstructed contrasts for the 3D simulation.

5.3.1. Contrast-source

First off, observing the reconstructed contrast-source, there are a lot of small details towards the front of the breast (the top of the image), which are not reconstructed well. The structure itself is visible, but the reconstructed values are around a magnitude of 2000 (abs), whereas the original value is up to a magnitude of 6000 (abs), which is three times more.

Another difference between this reconstruction and the 2D simulation is that a birdcage was used, so the weak area of the electric field is in the center and is more or less circularly symmetric. Therefore a 'streak as it was visible in the 2D simulation is not visible here, and should not be visible on the contrast reconstructions, although the center will still be difficult to reconstruct.

5.3.2. Contrast

Three different contrast reconstructions have been computed using the above mentioned inversion methods, the absolute value, the permittivity and conductivity. These can be found in that order in Figures 5.11 and 5.12.

The results are of significantly lower quality compared to the 2D reconstructions, with notably the Helmholtz method struggling to reconstruct the discontinuities accurately. When looking at the absolute values of the reconstruction they still look relatively accurate overall, with a little distortion in the center. Also, there seems to be difficulty in reconstructing the large jump in contrast between the low contrast of the lungs and the very high contrast of the sternum. However, comparing this to the reconstruction of the permittivity and conductivity a number of artefacts and more major distortions can also be observed.

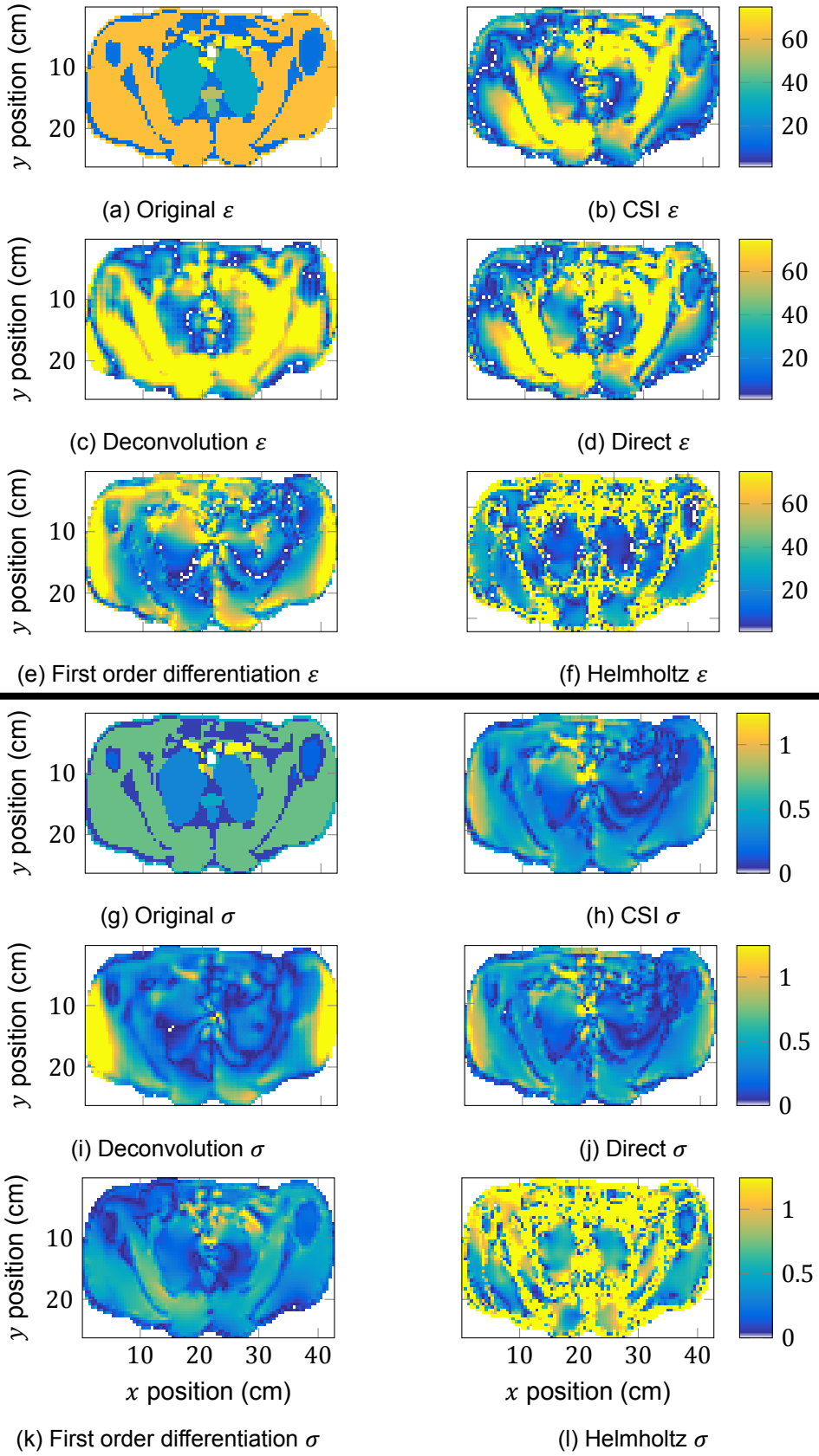

Figure 5.12: Permittivity ε and conductivity σ values of original and reconstructed contrasts for the 3D simulation. The original permittivity and conductivity can be found in Figures 5.12a and 5.12g. The reconstruction obtained using CSI in Figures 5.12b and 5.12h, those using the deconvolution approach in Figures 5.12c and 5.12i, those using the direct method in Figures 5.12d and 5.12j, those using first order differentiation approach in Figures 5.12e and 5.12k, and those using the Helmholtz based method Figures 5.12f and 5.12l.

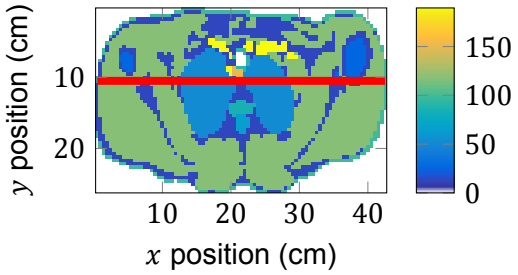

Figure 5.13: Absolute value of original contrast of 3D slice. Red line indicates location of cut-out.

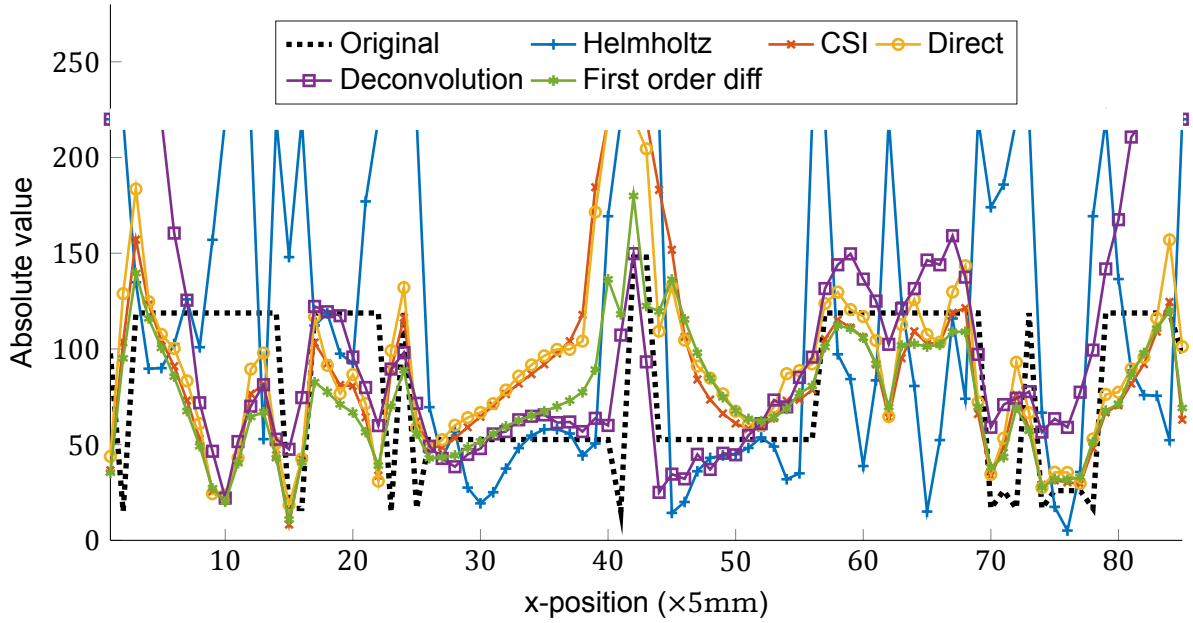

Figure 5.14: Absolute value of reconstructed and original contrast at location of cut out as indicated in Figure 5.13. Some reconstructions have been truncated at 220 to declutter the graph.

These artefacts show a significant drop in value, with a sharp edge. Therefore, it is believed these lines stem from the same sort of phase mismatch, caused by the relation between conductivity and permittivity, which shows that the polarisation assumption does not seem to hold very well inside the contrast in 3D at the edges of the scanner.

Another observation that can be made are the very bright sides of the deconvolution reconstruction (most clearly visible in the absolute value of the reconstruction). These are caused by the close proximity of the bird cage to the edges of the measured contrast. The large magnitude of the field right next to the contrast seems to influence the reconstruction, possibly because they are ‘smeared’ into the contrast through the filtering that is applied before deconvolution.

5.3.3. Reconstructions along a line

To give a more in depth view of the actual quality and accuracy of the reconstructions, we focus on reconstructions obtained along a line through the 2D contrast profile as illustrated in Figure 5.13. The values of the reconstruction at this profile can be seen in Figure 5.14.

The Helmholtz, CSI, direct and deconvolution reconstructions have been truncated at a magnitude of 220 to declutter the graph. The Helmholtz reconstruction has also been scaled so that the homogeneous parts of the contrast line up with the actual values. This is not

necessarily the case, but makes comparison easier between the methods.

In this line profile, it can clearly be observed that most methods have trouble reconstructing the center peak, except for the deconvolution and first order differentiation methods. An interesting point is also the dip most reconstructions display around x-position 62. This is most likely due to the dip in contrast one voxel above this point (in the y-direction) that can also be observed in the overview image of the original contrast. This displays the influence of the contrast on neighbouring voxels, which is probably also the case in the z-direction in 3D (possibly slightly smaller, due to the background field polarisation), which also could explain some artefacts.

5.4. In vivo Reconstructions

Of the in vivo data the reconstructions can be found in Figure 5.15. The measurements are of a human head, which can also be seen from the reconstructions. Notable in this dataset is how noisy the Helmholtz reconstruction seems to be in relation to the other reconstructions. This can be attributed to the second (partial) derivative that is taken in this method, and has also been observed in the two-dimensional case with simulated noise. Also the smoothing effect of the deconvolution method as compared to the other methods is evident. As there is no original contrast available the accuracy can unfortunately not be checked.

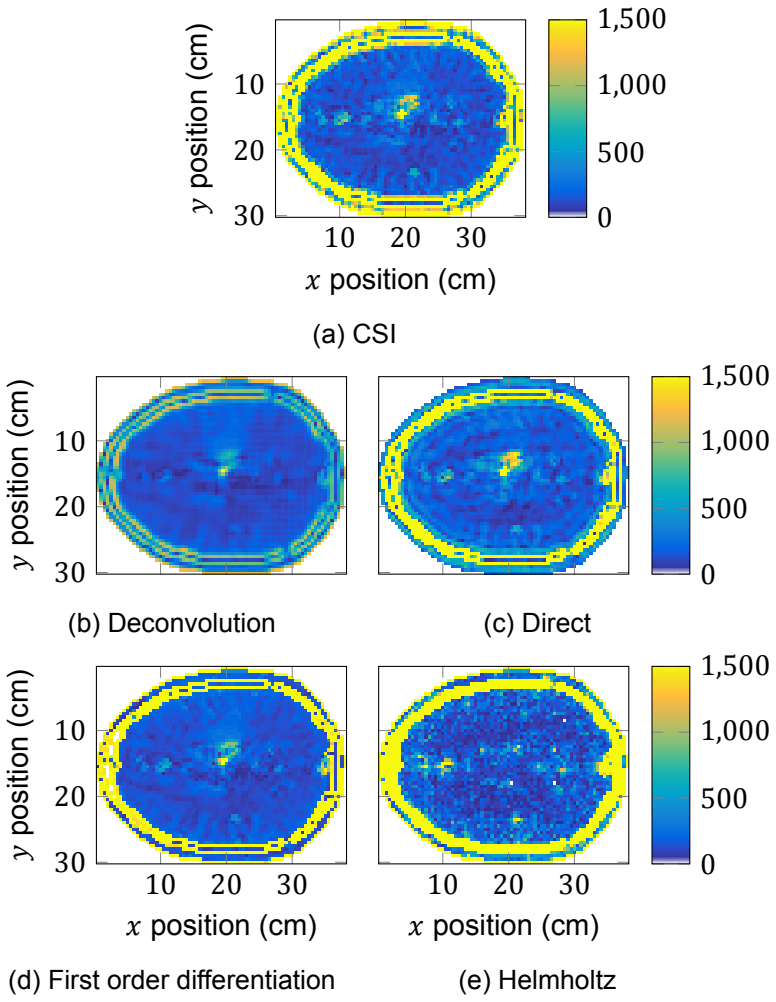

Figure 5.15: Absolute value of original and reconstructed contrasts for an in vivo measurement of a human head using a birdcage coil and a 3 Tesla scanner.

6

Discussion

In this chapter some assumptions regarding the 2D E-polarised field and contrast that were made are revisited with new information, or discussed critically in light of the subject matter. After this the domain of the measured B_1^+ and the information needed in a reconstruction are critically evaluated. Subsequently, perturbations and numerical rounding issues in a finite precision implementation are discussed.

6.1. Assumptions

A number of assumptions have been made during the course of this thesis and the derivation of reconstruction methods. Some of these will be revisited with knowledge gained through simulations, and others will be put to the test through rigorous analysis. The first assumptions made are those of a *linear, isotropic* and *time invariant* medium. These will be discussed here.

6.1.1. Linearity

One danger of an MRI scan is that the EM fields heat up tissue, which can be used in a beneficial way in hyperthermia. However, the electric properties of the dielectric tissue have a temperature dependence [14]. This means that these properties change as the tissue heats up. Now unfortunately there is currently no research into the exact dynamic influence of this during an actual MRI measurement as far as the author of this thesis is aware. However, this does point towards certain non-linearity in the tissue, and hence contrast. Once EPT methods have matured to the extend that they can provide accurate measurements on for example static dielectric phantoms this could be further investigated using in-situ measurements with real tissue.

6.1.2. Isotropic

As is already discussed by Katscher et al. [10] anisotropic examples of tissue can be found, e.g., for muscle or nerve fibers between the longitudinal and transverse direction [8]. However, it is currently still impractical to directly measure the different components. Nevertheless, the influence of this anisotropic component is only really a problem in the two-dimensional case when it influences the E-polarisation assumption. If a three-dimensional reconstruction algorithm would be used these anisotropic components could very likely be recovered with little extra effort.

Another interesting opportunity for future research would be to see in how far introducing an ‘artificial’ anisotropic component into the two-dimensional reconstruction methods (i.e. assume a certain anisotropy) could lead to better reconstruction of three-dimensional data since

these components can introduce the field vectors that are not taken into account through the E-polarisation assumption.

6.1.3. Time-invariance

Time-invariance is only considered during the time of the measurement. This is important, as evidently for example a young person growing up can change widely over the course of a number of years or even months. During this time the contrast would naturally change. But the real question is of course whether it changes during the time of a measurement. Real time measurements at time resolutions of 20 ms are a possibility [15]. Some (especially older) scanners still take a longer time to resolve the magnetic field accurately. However, even on longer timescales (seconds) the human body does not change to the extend that it would invalidate this assumption.

6.1.4. E-polarisation

As has already been shown in the reconstruction of a three-dimensional dataset in Section 5.3, the 2D assumption (naturally) does not hold very well there. Obviously not reconstructing the 3D components of the E-field (E_x, E_y) leads to an error when these are non-zero. The interesting observation however is that this error seems to come from a phase mismatch, leading to very large jumps. This seems to depend on the connection between conductivity and permittivity as when there is no conductivity the error disappears. This makes sense, as these are possibly coupled in much the same way as the electric and magnetic field are in the Maxwell equations. These were decoupled in the 2D E-polarised case, but will obviously be coupled again when the other field components are nonzero.

One way to deal with this issue is to derive the reconstruction methods for the case of a full three-dimensional field and coupled Maxwell's equations. However, the coupled equations will most likely lead to additional non-linearity, making the reconstruction more difficult. Another issue in the 3D case is the assumed E-polarisation of the background field, where a mismatch between the simulated field and the true field also influences the reconstruction.

6.2. Field domain

A note on the B_1^+ field that was used in the Helmholtz, the first order differentiation, and the deconvolution methods. In these methods the boundary condition for the contrast is not fully taken into account and will cause an error on the outer boundary. To more easily compare the overall reconstruction with the other methods, the B_1^+ field of the full simulated region is used as input for the reconstruction instead of just the field inside the area of the contrast (as it would be measured in real life). In Figure 6.1 the difference between the reconstruction with 'masked (true) field and with the 'full field can be observed.

6.3. Operator mismatch

A measure of robustness of a method is how sensitive it is to a perturbation on the data. In the case of the first order differentiation method this is equal to a perturbation in the operator. A magnitude mismatch of 10% can be observed in Figure 6.2. In Figure 6.2b the differencing operator (as defined in Equation (3.27)) is multiplied by 0.9. Because of this a line appears slightly below the centre on the left in the reconstruction. This line is white because all values < 0 are white with the given colormap of the figure. However, the numerical values of this line are negative.

Because of the large jump in reconstructed values it looks like the first order differentiation approach is sensitive to perturbations on the measurement. However, 10% is a large perturbation, and the rest of the reconstruction is still very recognisable.

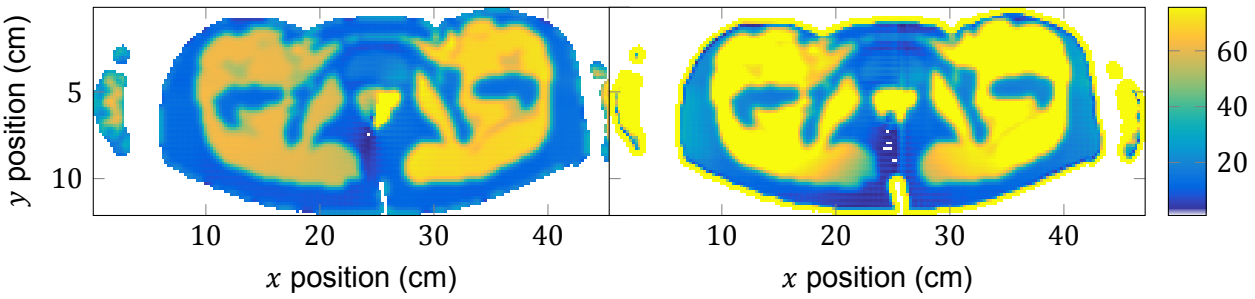

(a) Non-masked field permittivity reconstruction using the deconvolution method.

(b) Masked field permittivity reconstruction using the deconvolution method.

Figure 6.1: Comparison of the effect of masking the measured field on the reconstruction of the contrast using the deconvolution method.

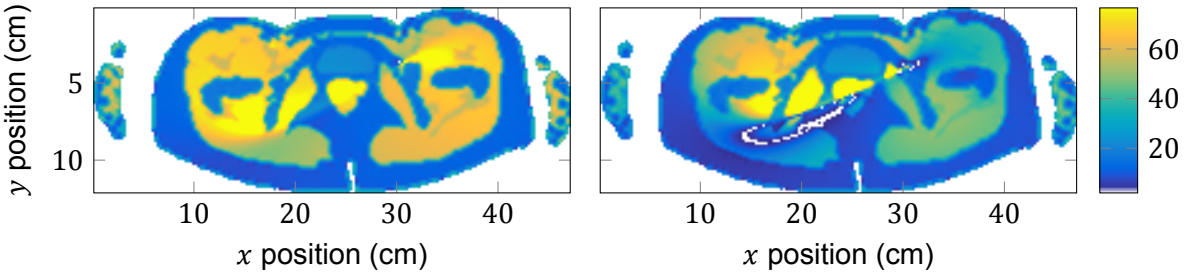

(a) No operator mismatch, $P = P$.

(b) Operator mismatch, $P = 0.9P$.

Figure 6.2: Permittivity of first order differentiation reconstruction with operator mismatch.

When investigating analytically the influence of this perturbation the biggest influence it has is in Equation (3.30). Here the right-hand side is scaled by 0.9 except the background field. In the last step of the reconstruction the scaling factor is compensated again (since it also scales the total field that is reconstructed), except for the fact that the background field is not scaled. This mismatch between the background field and a scattered field (with scatterer $\chi + 1$ instead of χ), is what most likely causes the reconstruction error.

To further investigate this, another reconstruction with a mismatch was carried out, only now in a forward simulation where the conductivity is set to 0. The reconstructed permittivity should still have the same values, so this will show what influence the two variables have on each other (since they are both part of the complex valued contrast). This reconstruction can be seen in Figure 6.3.

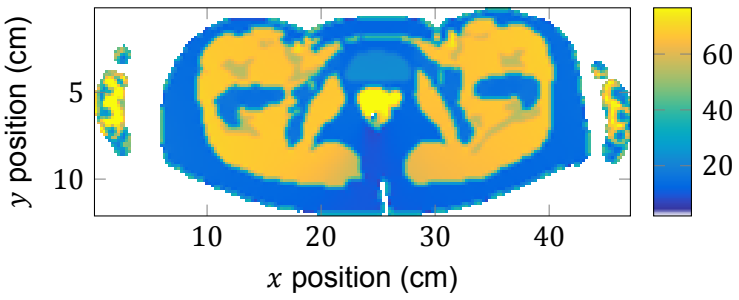

Figure 6.3: Operator mismatch, $P = 0.9P$. No conductivity in original contrast χ.

As is clear from Figure 6.3, the reconstruction is (almost) perfect. So even with a mismatched operator, when there is no interplay between the real and imaginary parts of the contrast the reconstruction is much easier. Another consequence the lack of conductivity has, is that the influence of the background field is diminished (compared to the scattered field), which also lead to less influence from an operator mismatch.

In the three-dimensional case these large jumps also appear, most likely caused by phase mismatches or errors between the contrast (source) and the background field through the fact that the E-polarisation assumption does not necessarily hold inside the contrast when the conductive medium interacts with the incident field.

6.4. Numerical issues

While working on these methods one problem became apparent relatively quickly. Rounding errors can have an impact on the quality of the final result. For example, given a fraction of two squares, one would consider the square of the fraction to be the same. However, with rounding errors, this is not the case, and can provide a noticeable increase in convergence (in terms of cost function values). That is to say

$$\underbrace{\frac{a^2}{b^2} = \left(\frac{a}{b}\right)^2}_{\text{analytical}} \rightarrow \underbrace{\frac{a^2}{b^2} \neq \left(\frac{a}{b}\right)^2}_{\text{numerical}}. \tag{6.1}$$

This means that when implementing these schemes numerically the utmost care must be taken to make sure no unnecessary scaling, multiplication or divisions are done, or the order of operations is chosen to minimise rounding errors This especially gets interesting when also trying to optimise for speed, as it is not always possible to do both.

7

Conclusion

First the different reconstruction methods are discussed, after which some concluding remarks on the reconstruction of EPT from MRI measurements are made.

7.1. Comparisons

The different methods are compared on four aspects, speed, accuracy, robustness, and flexibility. Some of these are more qualitative and others quantitative. An overview of the results is also tabulated in Table 7.1.

Speed The currently most widely used method, the Helmholtz method, is very fast. It requires one second derivative (which can be done with a matrix multiplication), and furthermore only element-wise division. The time needed to calculate the contrast with this method is almost negligible on most modern computers, even with a high resolution scan.

The first order differentiation method only requires a single derivative to get to the contrast source. However, to reconstruct the total field takes slightly longer, therefore it is marginally slower than the Helmholtz method.

Now the original CSI method is, due to being an iterative method, variable in speed. To get comparable results in accuracy to the other methods takes a little longer, due to calculating all the cost functions in the update procedure. The diagonalised CSI method performs slightly better, but still underperforms the others in terms of speed.

The direct method uses an iterative scheme, but these iterations are faster and the result also converges faster than CSI. When minimising not to the 2-norm but the 1-norm this method loses a lot of speed due to the difficulty of this and the extra iteration steps.

Lastly, the deconvolution method performs really fast as it only requires a single division, and then one scatter field has to be calculated to arrive at the final contrast. This makes it slightly faster than the first order differentiation method, as the total field is found more straightforward from the contrast-source than it is from the differenced B_1^+ field.

A quantitative time comparison can be found in Table 7.1.

Accuracy The Helmholtz method needs as previously mentioned the assumption of a constant contrast. That this introduces errors can clearly be seen in Figure 5.4f. The Helmholtz method matches up on the flat (constant) pieces accurately, but at all the boundaries, and slightly more heterogenous parts, it fails completely. Its accuracy therefore can vary widely depending on the subject and specific area under investigation.

The first order differentiation approach does not have this problem. We observe from Figure 5.4e that it almost perfectly reconstructs the contrast, even better so than the contrast source based methods. This is probably because it tries to solve the inversion problem analytically, instead of minimising a cost function.

The contrast source inversion method is very accurate as was also demonstrated by Balidemaj et al. [3]. Besides the discrepancies in the centre of the reconstruction, which is due to the lack of information since there is very little field strength, the results are fairly accurate. However, when applied to 3D data it becomes clear that this is a 2D operation. There is a noticeable decrease in accuracy in this case. If one were to derive the CSI formalism for 3D operators this could be improved upon greatly.

The direct method performs very comparable to the CSI method. Besides some minor differences the reconstructions are almost identical. These minor differences are most likely due to the different number of iterations (and thus convergence) of the methods.

Finally, the deconvolution method loses some accuracy due to the apodisation step required. Especially the discontinuities are averaged out, resulting in a blurry reconstruction. However, even though the reconstruction is blurry the contrast is still very well recognisable and there are no noticeable artefacts introduced by this method.

A quantitative analysis of the errors (for the 2D case) can be found in Table 7.1.

Robustness (noise) Inherently a method based on derivatives will not be able to cope well with noisy data. This is due to the noise being increased instead of averaged out as it is in integral based methods.

As can also be seen from the data, the Helmholtz method performs worst. Interesting enough however, the noise does not seem to influence the single difference method more than it does the contrast source based methods (at the same number of iterations as was used for the original reconstruction). However, the first order differentiation has (besides filtering the measured data) no way to deal with noise, whereas the contrast source based methods do.

The contrast source type methods are based on integral equations, so any noise that is there will be averaged over the domain, possibly decreasing its influence. Furthermore, and most importantly, both the CSI and direct methods allow for regularisation.

This regularisation will smooth the end result (as filtering the data would also do) but without loss of source information. Examples of this can be found in Figure 5.7 for example. This makes these methods more robust than the first order differentiation method.

The deconvolution method does not seem to be influenced by noise at all, but this is because filtering is applied at the offset already, so source information is lost at the advantage of robustness against noise.

Flexibility (regularisation etc.) As stated before, the CSI based methods are much more flexible than the differencing based ones. Besides regularisation these methods can also be extended with preconditioners to for example speed up the convergence or the calculation time per iteration.

Additionally, besides regularisation for noise there is also the possibility to regularise for specific contrast properties i.e. discontinuous transitions through the 1-norm in direct or total variation regularisation in the CSI method.

7.1.1. Choice of method

With the advantages and disadvantages of the methods given, which method seems to be most suitable for EPT? Both the first order differential and direct methods provide a very good accuracy at high speed. Of these methods, the first order differential method is slightly more

Method	Speed (seconds)	Accuracy (normalised)	Robust	Flexibility
Helmholtz	0.0028	2.278	-	-
First order diff.	0.0961	0.111	+	-
CSI (1000 iterations)	43.5540	0.328	+	+
Direct (50 iterations)	1.1649	0.258	+	+
Deconvolution	0.0214	0.565	++	-

Table 7.1: Quantitative and qualitative comparison between reconstruction methods. Accuracy is given in terms of the error as defined in the results chapter and on the 2D data reconstruction.

elegant from a mathematical point of view, but ultimately the flexibility and robustness that the direct method brings to the table makes it the most promising candidate of them all in my opinion.

7.2. Concluding remarks

What are the main takeaways from this research? Besides giving insight into new inversion methods, all of which have pros and cons, I believe the biggest takeaway is the approach to inversion. Before elaborating on this let us take a look at the two major reconstruction methods of this thesis.

First order differentiation provides a surprisingly robust, accurate and extremely fast way to get insight into the data. And the direct reconstruction method provides an incredible range of flexibility in its application, which has much potential for future research and implementation.

Finally, first order differentiation and direct reconstruction rely on as little assumptions in regards to the EM fields and the contrast as possible. This means that the result should be correct in a wide variety of cases and situations. Also, since they are based directly on the EM formulations of Maxwell's equation and scattering formalisms they are very insightful in regards to how the data interacts, the coupling between conductivity and permittivity and rotation of the field when measuring the B_1^+ field.

The importance of this is further illustrated by the results on 3D simulated data, where clearly, when the assumptions do not hold anymore errors and artefacts start to be introduced.

Especially if the goal is to reconstruct the electric properties accurately we cannot rely on simulations and the measurements of permittivity and conductivity in deceased tissue to give us a measure of accuracy, we need to know our inversion methods are accurate and rely on the values they provide.

7.3. Future work

Research is never finished, but a masters' thesis does come to an end. Therefore, unfortunately there is much left to be said and done. A short list of points that have come up during the work on this thesis is:

1. Three-dimensional: Rewrite these into 3D scattering formalisms and investigate possible sources for error, and derive the 3D equations for all methods (and the 'nabla Green's' function) and implement and test these.
2. Preconditioning: Investigate preconditioners for both contrast source inversion and the direct method to increase convergence speed.
3. Regularisation: Investigate other forms of regularisation to improve the discontinuous boundary reconstructions.

4. Speed: Take a critical look at the (computational) implementation of the methods and see if these can be improved upon.
5. True conductivity checks on larger data sets: more phantom measurements are necessary over a range of conductivities, permittivities, but also dielectric phantoms that contain a complex contrast (due to the coupling this might lead to).
6. Higher resolution: Look into applying these methods to 1mm or sub 1mm resolution datasets and see if they still perform as well, how does speed scale for example?
7. Integrate the RF shield in Green's operator.

These are the major areas, of which the three-dimensional extension of this work is indubitably the most important. I hope this thesis helps others getting a head start in this area and provides a good overview of possibilities.

A

Nomenclature

The nomenclature used throughout the thesis is shown in table Table A.1.

Quantity	Notation
Scalar	a
Vector	$\mathbf{a}$
Matrix	A
Lexicographical ordering	$\mathbf{a} = \mathrm{vec}(\mathrm{A})$
Field quantity (vector)	$\mathbf{A}$
Field quantity (i-dim)	A_i
Matrix transpose	A^T
Matrix hermitian	A^H
Identity matrix ($P \times P$)	I_P
Complex conjugate	$\overline{a}$
Partial derivative to i	∂_i
Nabla operator	$\nabla = [\partial_x, \partial_y, \partial_z]^T$
Real part	$\Re\{a\}$
Imaginary part	$\Im\{\cdot\}$
Imaginary unit	$\mathrm{j}^2 = -1$
Frequency domain quantity	$\hat{a}$
Temporal Fourier transform	$\hat{f}(\mathbf{x}, \omega) = \mathcal{F}\{f(\mathbf{x}, t)\}$
Angular wave domain quantity	$\tilde{a}$
Spatial Fourier transform	$\tilde{f}(\mathbf{k}, t) = \mathcal{F}\{f(\mathbf{x}, t)\}$
Inverse Fourier transform	$\mathcal{F}^{-1}\{\tilde{f}(\mathbf{k}, t)\} = f(\mathbf{x}, t)$
Domain	$\mathcal{D}$ or $\mathcal{B}$
Inner product on $\mathcal{D}$	$\langle f, g\rangle_{\mathcal{D}} = \Re\left[\int_{x\in\mathcal{D}} f(x)\overline{g}(x)\,\mathrm{dV}\right]$
P-norm	$\|\cdot\|_p$
Norm on $L^2(\mathcal{D})$	$\|f(x)\|_{\mathrm{D}}^2 = \langle f, f\rangle_{\mathcal{D}}$
Green's function	$G\{\cdot\}$
Green's operator	$G(\cdot)$

Table A.1: The nomenclature used in this document.

B

Algorithms

In this appendix the different inversion algorithms are summarised.

B.1. Contrast source inversion

The CSI-EPT algorithm is reproduced here as it is describe in [3] with regularisation.

Algorithm 1: CSI-EPT with regularisation

Data: B_1^+, E_z^{b} field
Result: Reconstructed contrast χ and total field E_z
compute initial contrast source $w_r^{[0]}$ and nonzero contrast $\chi^{[0]}$;
for $n = 1$ **to** k **do**
    Step 1: *Update the contrast source*;
    begin
        1. Compute the gradient of the objective function with respect to w_r at $w_r = w_r^{[n-1]}$ and $\chi = \chi^{[n-1]}$;
        2. Compute $v^{[n]}$ the Polak-Ribière update direction;
        3. Compute the step length $\alpha^{[n]}$;
        4. Determine the new contrast source $w_r^{[n]} = w_r^{[n-1]} + \alpha^{[n]} v_r^{[n]}$;
    end
    Step 2: *Update the contrast function*;
    begin
        1. Compute the preconditioned gradient of the objective function with respect to χ at $w_r = w_r^{[n]}$ and $\chi = \chi^{[n-1]}$;
        2. Compute $d^{[n]}$ the Polak-Ribière update direction;
        3. Compute the step length $\alpha_\chi^{[n]}$;
        4. Determine the new contrast source $\chi_r^{[n]} = \chi_r^{[n-1]} + \alpha_\chi^{[n]} v_r^{[n]}$;
    end
    if $F^{[n]}$ < *user defined tolerance* **then**
        return χ, E_z
    else
        Continue
    end
end
return χ, E_z

B.1.1. Diagonalised CSI

In diagonalised CSI the contrast update step is foregone (steps 11-16) and instead a regularisation parameter η is updated every iteration as

$$\eta^{[n]} = \frac{w^{[n]}\overline{E}_z^{\mathrm{b}}}{|E_z^{\mathrm{b}}|^2}, \tag{B.1}$$

which is used in the algorithm. This is the only difference between the two methods.

B.2. Single step methods

All of the single step methods follow the same procedure, which can be found in Algorithm 2. How the contrast-source is reconstructed, however, differs between the two, which is described separately below.

Algorithm 2: Single-step algorithm procedure

Data: B_1^+, E_z^{b} field
Result: Reconstructed contrast χ and total field E_z
Require: G_S, G_D
1 $w \longleftarrow$ `ComputeContrastSource(`B_1^+, G_S`)`;
2 $E_z \longleftarrow E_z^{\mathrm{b}} + G_D\{w\}$;
3 $\chi \longleftarrow \frac{w\overline{E}_z}{|E_z|^2}$;
4 **return** χ, E_z

B.2.1. Deconvolution

The deconvolution function to reconstruct the contrast-source can be found in Algorithm 3.

Algorithm 3: Deconvolution function to reconstruct the contrast-source

1 **Function** `ComputeContrastSource(`B_1^+, G_S`)` **is** `/* algorithm to reconstruct the contrast-source using the deconvolution method */`
  Data:
  B_1^+: Measured B1 field
  G_S: Greens operator to relate contrast source to B1 field (Generally G^{∇} will be used)
  Result: w: contrast-source
  Require: Apodisation matrix D, medium parameters c
2 $\tilde{B}_1^+ \longleftarrow \mathcal{F}\{B_1^+\}$; `/* Take the Fourier transform */`
3 $\tilde{B}_A \longleftarrow D\tilde{B}_1^+$; `/* Apply apodisation */`
4 $\tilde{w} \longleftarrow c\frac{\tilde{B}_A}{G_S}$; `/* Deconvolution */`
5 $w \longleftarrow \mathcal{F}^{-1}\{\tilde{w}\}$; `/* Inverse Fourier transform */`
6 **return** w
7 **end**

B.2.2. Minimum norm

The function to reconstruct the contrast-source through the minimum norm solution can be found in Algorithm 4. In the next sections the minimisation algorithms are described.

Algorithm 4: Minimum norm method to reconstruct the contrast-source

Function `ComputeContrastSource(`B_1^+, G_S`)` **is** `/* algorithm to reconstruct the contrast-source using the minimum norm method */`
  Data:
  B_1^+: Measured B1 field
  G_S: Greens operator to relate contrast source to B1 field (Generally G^∇ will be used)
  Result: w: contrast-source
  switch p, *type of norm* **do**
    case $p = 2$ **do**
      $w \leftarrow$ `LSQR(`$G_S\{w_{est}\} - B_1^+$`)`
    end
    case $p = 1$ **do**
      $w \leftarrow$ `IRLS(`$G_S\{w_{est}\} - B_1^+$`)`
    end
  end
  return w
end

B.2.3. Norm minimisation algorithms

Two different algorithms are used to find the least squares solution. First, for the ℓ_2 norm the LSQR is used, this is also used to solve the least squares problem posed in the IRLS algorithm which iterates over this to solve for the ℓ_1 norm.

LSQR

Algorithm 5: LSQR Algorithm

Function *IRLS* **is**
  1. Initialise;
  for *i=1,2,3,…* **do**
    2. Continue the bidiagonalisation;
    3. Construct and apply next orthogonal transformation;
    4. Construct and apply next orthogonal transformation;
    5. Update x, w;
    6. Test for convergence;
    if *Converged* **then**
      exit;
    else
      Continue;
    end
  end
end

IRLS

Algorithm 6: IRLS Algorithm

Function *IRLS* **is**
  for *k=1,2,3,…* **do**
    $r_i^{(k)} = (b - Ax^{(k)})_i$;
    $D_k = \mathrm{diag}((|r_i^{(k)}|)^{(p-2)/2})$;
    Solve $\delta x^{(k)}$ from $\min_{\delta x} \|D_k(r^{(k)} - Ax^{(k)})\|_2$;
    $x^{(k+1)} = x^{(k)} + \delta x^{(k)}$;
  end
end

C

Matlab

In this chapter a number of Matlab® implementations of algorithms and operators are described to improve reproducibility of this research.

C.1. Operators

C.1.1. Weak Green's operator

To use the Green's operator in 2D (and 3D) it needs to be weakened because of its logarithmic singularity. To do this the weak Green's function is introduced as

$$G^w(\mathbf{x}) = -\frac{1}{\pi a^2}\int_{\mathbf{x}'\in\mathbb{D}^{\text{circ}}} G(\mathbf{x}-\mathbf{x}')\,\mathrm{d}A, \tag{C.1}$$

Where $\mathbb{D}^{\text{circ}}$ is the domain of a circle with radius a centred at the origin (where the original singularity lies). Following [12] this yields the following equations for $\mathbf{x}$ outside of the singularity (non-self patch elements)

$$G^w(\mathbf{x}) = -\frac{\mathrm{j}}{2k_b a}J_1(k_b a)H_0^{(2)}(k_b|\mathbf{x}|), \tag{C.2}$$

and inside the (previously) singular region (self patch elements)

$$G^w(\mathbf{0}) = -\frac{\mathrm{j}}{2k_b a}\left[H_0^{(2)}(k_b|\mathbf{x}|) - \frac{2}{\pi k_b a}\right]. \tag{C.3}$$

Here k_b is the wavenumber, a the radius of the circular disk used to circumvent the singularity, J_1 and $H_0^{(2)}$ Bessel functions and $\mathbf{x}$ the grid points the Green's operator is defined on. To generate the numerical form of this is fairly straightforward with a coordinate mesh generated with for example meshgrid and then using the besselj and besselh commands for the Bessel functions.

C.1.2. 'Nabla Green's' operator

The nabla Green's operator as it was found in Equation (4.4) is equally straightforward to implement as the weak Green's operator. Care must be taken that the right bessel functions are used, but besides that there is little difficulty in this.

C.1.3. 'Rotation' operator

The rotation operation is the combination of a single partial differentiation in the x dimension and a single partial differentiation in the y dimension multiplied by the imaginary unit j.

This can be done in one matrix multiplication by making a differencing matrix as described in [12]. The operator in this case will look like

$$\text{'Rotation'} = c\left[(Y \otimes R_m) + \mathrm{j}(R_n \otimes TX)\right], \tag{C.4}$$

where c is a scaling operator based on the mesh size and medium parameters. In Matlab® the differencing matrices X and Y can be constructed using the spdiags function, and the Kronecker product is implemented in the kron function.

C.2. Functions

A number of functions is used to calculate both the action of the operators on fields as well as do the minimisations required for certain algorithms.

C.2.1. Vector potential

The action of the Green's operators on vector fields can be calculated using FFTs. This is a very powerful and fast way to calculate the convolutions. In Matlab® I have implemented these with the operators already in the Fourier domain, so that this operation does not need to be performed every time. This is useful since in the iterative schemes this operation will be calculated at least once for every iteration. The rest is fairly straightforward, an example is presented in Listing 4.1.

Listing C.1: Green's function

```
function field = greensFun(operator, source)
    % compute dimensions
    dim = size(source); fftDim = size(operator);
    % pad input for FFT
    source = padarray(source,fftDim-dim,'post');
    % perform discrete convolution using FFT
    field = ifft2(operator .* fft2(source));
    % reshape output
    field = field(1:dim(1),1:dim(2));
end
```

C.2.2. Least squares functions

The core of the direct algorithm centers on minimising a least squares problem. In Matlab® this was done using the LSQR algorithm [11]. A number of difficulties arise in doing this.

First of all, the input (and output) of the function to be minimised must be vectors. We can use lexicographic ordering on the 2D field or contrast matrix to make vectors out of these.

Then, LSQR requires the adjoint of the function that is minimised over. If this were a simple vector this would be easy, unfortunately, we are dealing with a convolution using FFTs.

To remedy this problem one needs to define a transpose operation of the circular deconvolution. Numerically speaking this means the time-reversed complex conjugated shifted by one kernel. When using the normal 'weak' Green's operator simply taking the hermitian is sufficient. However, when dealing with the 'nabla Green's operator this must be taken into account. One way to do that is use the rot90 operator. A more thorough explanation of this can be found in [].

C.3. Data formats

While working with all these different schemes and methods I found it very useful to think about the input (and output) data formats so that all of them could be used with the same inputs and the plotting routines would work with the same results.

There are two major ways to deal with large combined data objects in Matlab®. The first would be cell arrays (or structs). Structures are basically cell arrays with named cells, these provide more insight into the data contained within them by being descriptive. The second are classes.

Before going into classes let me explain why I think these data objects are important. For example, when reading data in, you will have a matrix of (complex) field measurements. For this measurement you also have a mesh size or resolution ($a \times b$ mm), and an overal size (which can be derived from the matrix size of course). You may also want to combine this with a mask for the data in the case of simulations, as in a real scanner you do not have access to data outside the object. And when using EM based inversion methods you also need a simulation or measurement of the incident or background field.

All of these matrices and values are related in a single measurement. Therefore it makes sense to store them together. This way there is no confusion as to which variable belongs to which measurement.

Storing them in structs means you can use the dot notation to call on different parameters as data.measuredField = b1+ and data.deltax = dx for example. This way both the mesh size in the x direction and the field are contained in the data variable (this can be extended to contain all important parameters of course).

Now structs are nice since they are easy to implement, but taking this one step further is also interesting. Making an MRI-data class for example would mean that you could implement automatic display calls to not display the full matrix but only relevant parameters, ease plotting routines by overloading standard Matlab® operators and automatically add certain parameters such as size, without explicitly calling this command on the field size.

Of course implementing a class is much more work, but when dealing with a lot of different datasets I would suggest it as a possibility. Setting it up is a one time investment, and after that it should make a lot of operations easier (even the reconstruction methods).

D

Discretisation

To be able to apply the inversion methods that are described in this thesis on real data, both the methods as well as the computational domain need to be discretised. After this it becomes possible to numerically apply the methods and approximate the analytic relations describing them. To carry out this discretisation procedure first the geometry of the problem will be discretised, and after this the operators and equations are discretised.

The discretisation will only be described in brief, but a lot of reference material can easily be found when a more in depth discussion is needed. Much of the discretisation will be based on [12, 21], in which also more literature on this subject can be found.

D.1. Discretising of the geometry

The geometry will be discretised using a vertex centred uniform grid. Uniform means that the x- and y- step sizes are equal and will be denoted with $h = \Delta x = \Delta y$. The grid size h will be equal to the resolution of the measurement (or model in the simulations). Vertex centred means that the position of the unknowns (and in this case also the measurements) is on the vertices of the grid.

One last note on the grid is that the origin is chosen at the top left, with the x-axis increasing to the right and the y-axis increasing towards the bottom of the grid. This is the same as horizontally flipping a regular cartesian grid and is done due to the nature of the imagesc command in Matlab®which orders the (gridded) values of a matrix in this way. This way the grid corresponds with the images shown in this thesis.

A schematic representation of this can be found in Figure D.1.

Sometimes these gridded variables are used as a vector variable. In these cases an x-lexicographical notation is used. To denote the 'vectorisation' of a variable the operator vec is used as notation. Given matrix A

$$A = \begin{pmatrix} a_{1,1} & a_{2,1} & \cdots & a_{N,1} \\ a_{1,2} & a_{2,2} & \cdots & a_{N,2} \\ \vdots & \vdots & \ddots & \vdots \\ a_{1,M} & a_{2,M} & \cdots & a_{N,M}, \end{pmatrix} \tag{D.1}$$

this results in

$$\mathrm{vec}(A) = \left[a_{1,1}, a_{2,1}, \ldots, a_{N,1}, a_{1,2}, \ldots, a_{N-1,M}, a_{N,M}\right]^T. \tag{D.2}$$

D.2. Discretising of the operators

There are two main components that need to be discretised. These are the Green's operator (or nabla-Green's) and the finite differencing that needs to be performed. Most of the

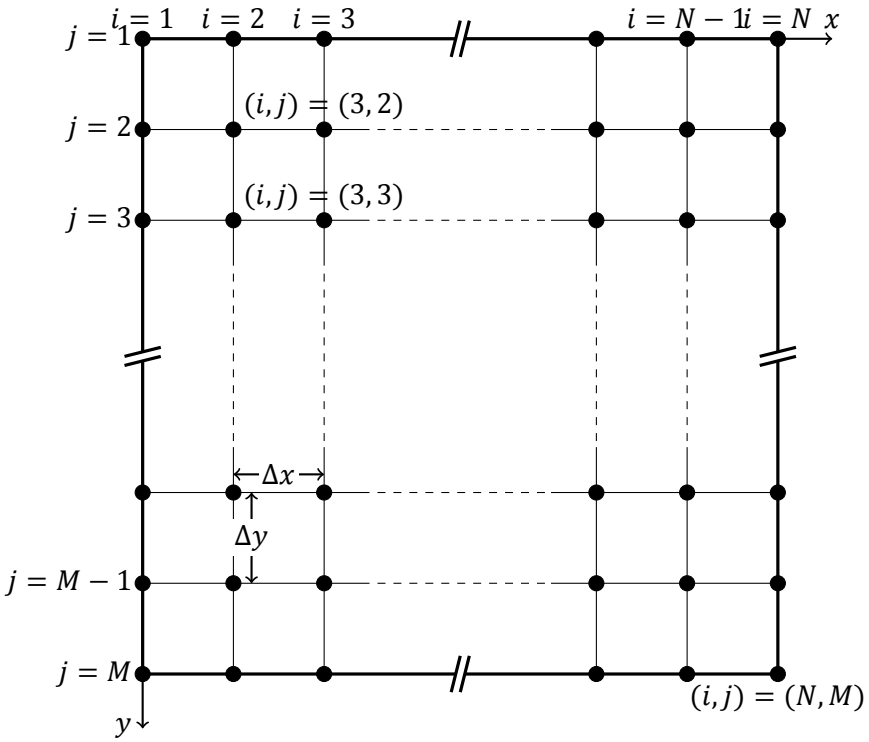

Figure D.1: Uniform vertex centred mesh as used in this thesis. N and M are the x and y sizes respectively, h is the grid size.

derivations in this section are based directly on [12].

D.2.1. Green's operator

We start with the analytic vector potential of Equation (2.35) repeated here for convenience

$$A(\mathbf{x}) = c \int_{\mathbf{x}' \in \mathbb{R}^2} G(\mathbf{x} - \mathbf{x}')\chi(\mathbf{x}')E(\mathbf{x}')\,\mathrm{d}V. \tag{D.3}$$

Here c is a constant depending on the medium parameters. Since there is a grid of variables and these aren't known continuously the right-hand side of above equation is used to approximate A at the grid nodes through position vector $\mathbf{x} = \mathbf{x}_{i,j}$ as

$$A(\mathbf{x}_{i,j}) = c \int_{\mathbf{x}' \in \mathbb{R}^2} G(\mathbf{x}_{i,j} - \mathbf{x}')\chi(\mathbf{x}')E(\mathbf{x}')\,\mathrm{d}V. \tag{D.4}$$

Assuming χ is piecewise constant within each discretisation cell allows to write

$$\chi(\mathbf{x}) = \chi_{m,n} \quad \text{if } \mathbf{x} \in \mathbb{S}_{m,n}, \tag{D.5}$$

where $\chi_{m,n}$ is position independent, and $\mathbb{S}_{m,n}$ is used to denote the area of the discretisation cell centred on $(x, y) = (m, n)$. This leads to

$$A(\mathbf{x}_{i,j}) = \sum_{n=1}^{M} \sum_{m=1}^{N} c\chi_{m,n} \int_{\mathbf{x}' \in \mathbb{R}^2} G(\mathbf{x}_{i,j} - \mathbf{x}')E(\mathbf{x}')\,\mathrm{d}V. \tag{D.6}$$

Now, to approximate the integral over the discretisation cells the midpoint rule is used to arrive at

$$A(\mathbf{x}_{i,j}) \approx c\Delta x\Delta y \sum_{n=1}^{M} \sum_{m=1}^{N} G(\mathbf{x}_{i,j} - \mathbf{x}_{m,n})\chi_{m,n}E(\mathbf{x}_{m,n}). \tag{D.7}$$

Note that the sum ranges from $n = [1, \dots, N]$ and $m = [1, \dots, M]$. Via two-dimensional FFTs Equation (D.7) can be evaluated very efficiently.

To do this the contrast vector $\mathbf{c}$ and matrix C are introduced as

$$\mathbf{c} = \mathrm{vec}(\chi_{m,n}) \quad \text{and} \quad \mathrm{C} = \mathrm{diag}(\mathbf{c}). \tag{D.8}$$

In addition the Green's operator is discretised by introducing the matrix $G_{m,i}$, for $m, i = 1, \dots, N$, of order M with elements

$$\left(G_{m,i}\right)_{j,n} = \Delta x \Delta y G(\mathbf{x}_{i,j} - \mathbf{x}_{m,n}), \tag{D.9}$$

for $j, n = 1, \dots, M$. This concludes the discretisation of the operators and equations needed for the single-step methods.

D.2.2. Differencing operator

For differencing a central differencing scheme is used

$$\partial_x A_z|_{\mathbf{x}=\mathbf{x}_{m,n}} \approx \frac{A_z(\mathbf{x}_{m+1,n}) - A_z(\mathbf{x}_{m-1,n})}{2\delta x}. \tag{D.10}$$

This discretised equation can easily be implemented numerically in a differencing matrix. To create such a matrix in for example Matlab® the spdiags command may be used as

```
e = ones(n,1);
T = 1/(2*dx)*spdiags([-e e], [-1 1], n, n);
```

where T is the differencing matrix which is expanded for the two-dimensional case (∂_x and ∂_y) using tensor products. These can be implemented in Matlab®with Kronecker products with the kron(A,B) command. The full operator then becomes (discretised)

$$\partial_y + \mathrm{j}\partial_x \approx \mathrm{D} = (\mathrm{T} \otimes \mathrm{I}_N) + \mathrm{j}(\mathrm{I}_M \otimes \mathrm{T}) \tag{D.11}$$

Where I_d is an identity matrix of dimension d. To apply this operation on the measured field, the field has to be vectorised (again with x-lexicographic ordering). This means that discretising PB_1^+ becomes

$$PB_1^+ \approx \mathrm{D} \cdot \mathrm{vec}(B_1^+), \tag{D.12}$$

where medium parameters and other scaling constants (e.g. due to cell size) are obviously taken into account in the D operator.

E

Comparison of different norm reconstructions using the direct method

To compare the influence of a changed norm two reconstructions of a $1\mathrm{mm}$ pixel sized Ella model have been computed. One of these is computed using the ℓ_2 norm LSQR approach, and the other using the ℓ_1 norm IRLS approach. The first can be found in Figure E.2a and the second in Figure E.2b. To further illustrate the difference between the two the difference is displayed in Figure E.2c. The reconstructions presented here were calculated in 5 minutes for the LSQR (ℓ_2) method and roughly 7 hours for the IRLS (ℓ_1) method.

A more in detail image can be seen in Figure E.1. Here the influence of the ℓ_1 norm at the boundary can be observed. Especially the high contrast on the right is smoother due to the properties of the ℓ_1 minimisation.

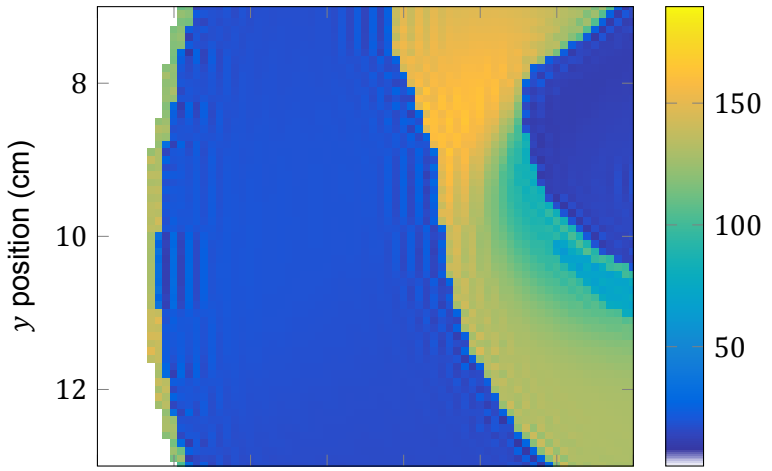

(a) Absolute value of ℓ_2 reconstruction χ_2.
Computed with 500 LSQR iterations

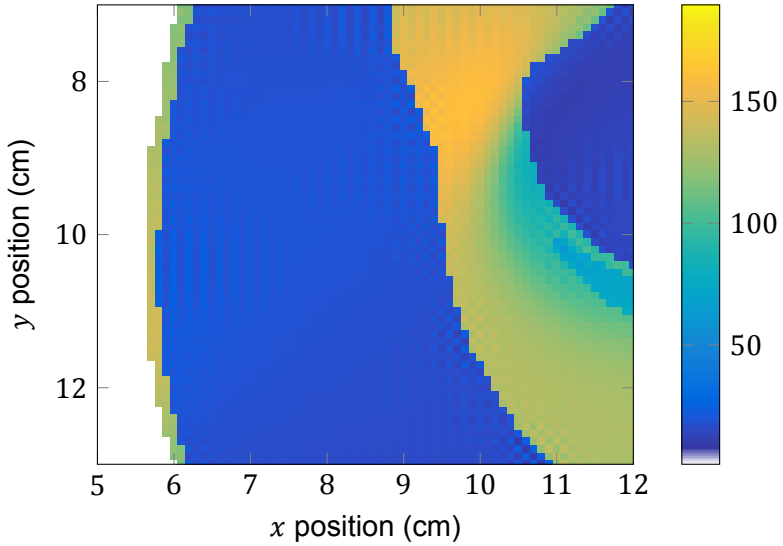

(b) Absolute value of ℓ_1 reconstruction χ_1.
Computed with 500 IRLS iterations (with 100 nested LSQR iterations).

Figure E.1: Comparison of ℓ_1 and ℓ_2 reconstructions using the direct method on a $1\mathrm{mm}$ pixel sized Ella model. This is just a zoomed in version of the reconstructions found in Figure E.2

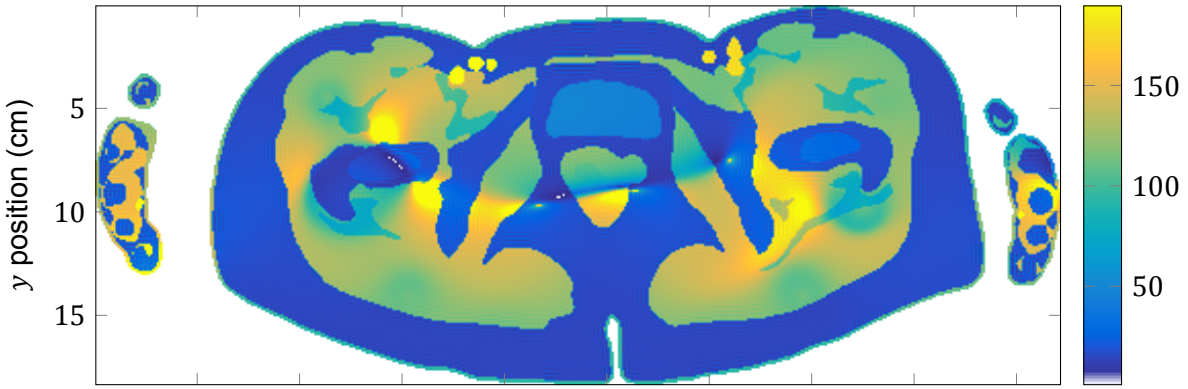

(a) Absolute value of ℓ_2 reconstruction χ_2. Computed with 500 LSQR iterations

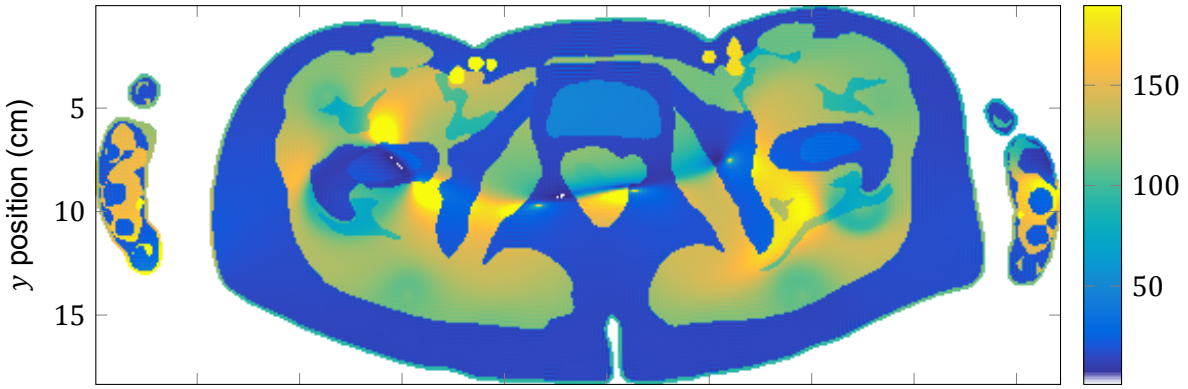

(b) Absolute value of ℓ_1 reconstruction χ_1. Computed with 500 IRLS iterations (with 100 nested LSQR iterations).

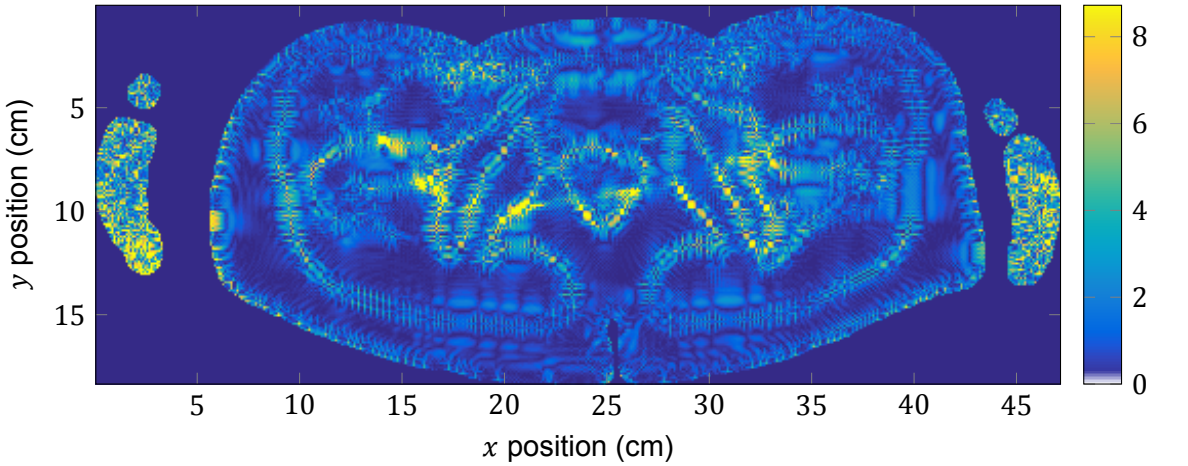

(c) Absolute value of difference between ℓ_1 and ℓ_2 reconstructions, $|\chi_2 - \chi_1|$.

Figure E.2: Comparison of ℓ_1 and ℓ_2 reconstructions using the direct method on a $1\mathrm{mm}$ pixel sized Ella model.

F

Phantom reconstructions

Measurements on phantoms have been used to see whether and how well the conductivity can be reconstructed. Unfortunately, the measurements on these phantoms were made some time ago in an older MRI scanner. This means that there is more noise on these datasets than on the in-vivo measurements, and due to an offset between amplitude and phase measurements (introduced by a software bug that has since been fixed) the data need to be slightly altered to be combined, further convoluting the measurement.

Nevertheless, these datasets have been treated with the same methods as described in the rest of this thesis, and the results of these reconstructions are presented here.

Since the background field is very weak in the interior of the phantoms, and this results in a bad reconstruction when using certain methods, a selection of the interior of the phantom is used to calculate the conductivity value instead of the whole interior. The red lines in Figure F.1 are used to indicate the area (between the red lines) used to average over to find the conductivity value for the phantom.

The graphed results for the reconstructed conductivity versus the actual conductivity can be found in Figure F.3. Scaling has been applied to the results to match the original conductivity. This scaling is uniform, the results were multiplied with a scalar.

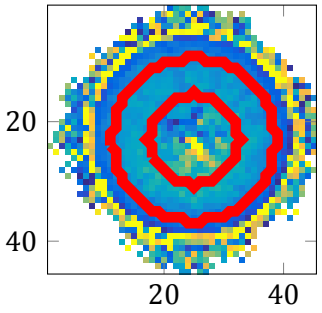

Figure F.1: Reconstructed absolute value of phantom contrast using the direct method.

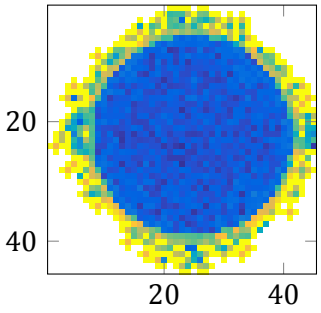

Figure F.2: Reconstructed absolute value of phantom contrast using the Helmholtz method.

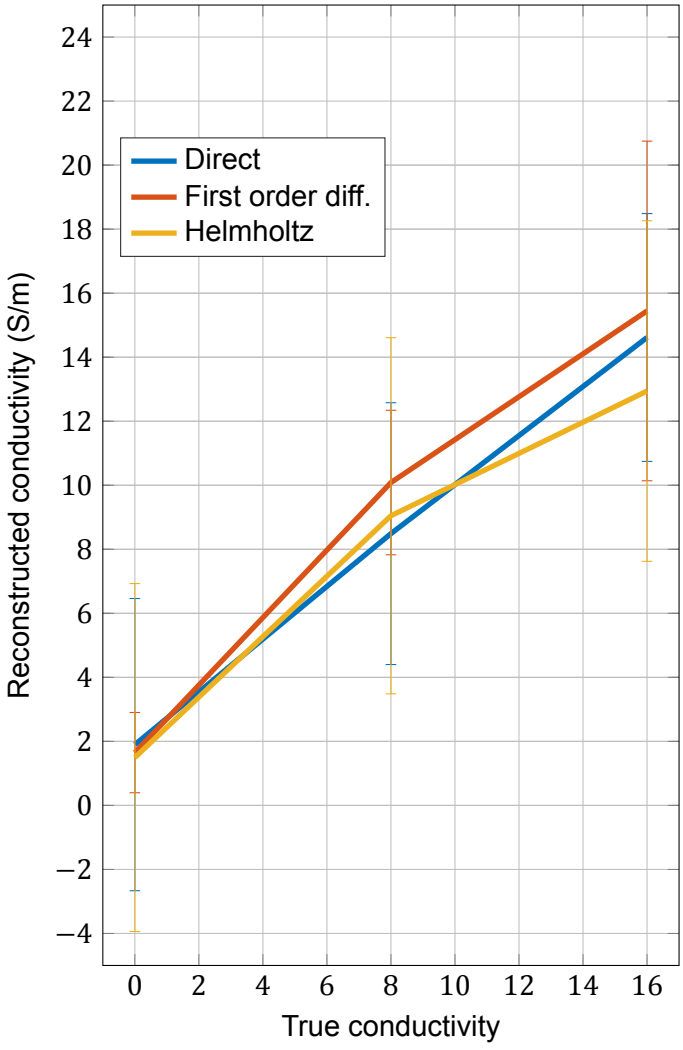

Figure F.3: Reconstructed conductivity values for three different methods. Error bars are equal to one standard deviation.

Glossary

apodisation Is an optical filtering technique, and its literal translation is ”removing the foot”. It is the technical term for changing the shape of a mathematical function, an electrical signal, an optical transmission or a mechanical structure. In optics, it is primarily used to remove Airy disks caused by diffraction around an intensity peak, improving the focus. iii, 11, 12, 38

CSI Contrast Source Inversion, a wave field inversion method that iteratively minimises a cost functional. iii, 10, 18, 21, 22, 37, 44

EM Electromagnetic is a type of physical interaction that occurs between electrically charged particles. 1, 3, 6, 33, 39

EP Electrical properties are the conductivity σ, permittivity ϵ, and permeability μ. 2

EPT Electrical properties tomography is an imaging modality to reconstruct the electric conductivity and permittivity inside the human body based on B_1^+ maps. iii, 1, 2, 13, 37, 38

hyperthermia A method of treating diseased tissue by heating it up through for example electromagnetic radiation. 2, 33

in vivo Studies that are in vivo are those in which the effects of various biological entities are tested on whole, living organisms usually animals including humans, and plants as opposed to a partial or dead organism, or those done in vitro (”within the glass”), i.e., in a laboratory environment using test tubes, petri dishes. iii, 17, 18, 32

MRI Magnetic resonance imaging is an imaging system used to measure the magnetic field inside the human body using the magnetic resonance of tissue. iii, v, 1, 3–6, 8, 20, 27, 28, 33, 37

phantom An artificial contrast source with known electric properties used to test MRI scanners. 17, 18, 21, 59

preconditioning Is the application of a transformation, called the preconditioner, that conditions a given problem into a form that is more suitable for numerical solving methods. Preconditioning is typically related to reducing a condition number of the problem. iii

regularisation In mathematics and statistics and particularly in the fields of machine learning and inverse problems, refers to a process of introducing additional information in order to solve an ill-posed problem or to prevent overfitting. iii, 12, 38, 39

RF Radio frequencies are frequencies inside the specific radiofrequency bandwidth. 4

SAR Specific absorption rate is a measure for how much energy is being dissipated inside tissue based on the field applied to it. 2

Bibliography

[1] A. Abubakar, T. M. Habashy, P. M. van den Berg, and D. Gisolf. The diagonalized contrast source approach: an inversion method beyond the born approximation. *Inverse problems*, 21(2):685, 2005.

[2] G. B. Arfken. Mathematical methods for physicists 3rd edn (orlando, fl: Academic). 1985.

[3] E. Balidemaj, C. A. van den Berg, J. Trinks, A. L. van Lier, A. J. Nederveen, L. J. A. Stalpers, H. Crezee, and R. F. Remis. Csi-ept: a contrast source inversion approach for improved mri-based electric properties tomography. *Medical Imaging, IEEE Transactions on*, 34(9):1788–1796, 2015.

[4] A. Björck. *Numerical methods for least squares problems*. Siam, 1996.

[5] W. Brink. *Non-Invasive Electromagnetic Ablation of Female Breast Tumors*. TU Delft, Delft University of Technology, 2010.

[6] A. Christ, W. Kainz, E. G. Hahn, K. Honegger, M. Zefferer, E. Neufeld, W. Rascher, R. Janka, W. Bautz, J. Chen, et al. The virtual family-development of surface-based anatomical models of two adults and two children for dosimetric simulations. *Physics in medicine and biology*, 55(2):N23, 2010.

[7] A. G. Filler. The history, development and impact of computed imaging in neurological diagnosis and neurosurgery: Ct, mri, and dti. *Nature Precedings*, 7(1):1–69, 2009.

[8] S. Gabriel, R. W. Lau, and C. Gabriel. The dielectric properties of biological tissues: Ii. measurements in the frequency range 10 hz to 20 ghz. *Physics in medicine and biology*, 41(11):2251, 1996.

[9] A. Guitton and W. W. Symes. Robust inversion of seismic data using the huber norm. *Geophysics*, 68(4):1310–1319, 2003.

[10] U. Katscher, T. Voigt, C. Findeklee, P. Vernickel, K. Nehrke, and O. Dossel. Determination of electric conductivity and local sar via b1 mapping. *Medical Imaging, IEEE Transactions on*, 28(9):1365–1374, 2009.

[11] C. C. Paige and M. A. Saunders. Lsqr: An algorithm for sparse linear equations and sparse least squares. *ACM Transactions on Mathematical Software (TOMS)*, 8(1):43–71, 1982.

[12] R. F. Remis and E. Charbon. An electric field volume integral equation approach to simulate surface plasmon polaritons. *Advanced Electromagnetics*, 2(1):15–24, 2013.

[13] R. Schmidt and A. Webb. A new approach for electrical properties estimation using a global integral equation and improvements using high permittivity materials. *Journal of Magnetic Resonance*, 262:8–14, 2016.

[14] H. P. Schwan and K. R. Foster. Rf-field interactions with biological systems: electrical properties and biophysical mechanisms. *Proceedings of the IEEE*, 68(1):104–113, 1980.

[15] M. Uecker, S. Zhang, D. Voit, A. Karaus, K.-D. Merboldt, and J. Frahm. Real-time mri at a resolution of 20 ms. *NMR in Biomedicine*, 23(8):986–994, 2010.

[16] P. M. Van Den Berg and A. Abubkar. Contrast source inversion method: state of art. *Journal of Electromagnetic Waves and Applications*, 15(11):1503–1505, 2001.

[17] P. M. Van Den Berg and R. E. Kleinman. A contrast source inversion method. *Inverse problems*, 13(6):1607, 1997.

[18] B. Van Den Bergen, C. C. Stolk, J. B. van den Berg, J. J. W. Lagendijk, and C. A. T. Van Den Berg. Ultra fast electromagnetic field computations for rf multi-transmit techniques in high field mri. *Physics in medicine and biology*, 54(5):1253, 2009.

[19] A. L. H. M. W. Van Lier. *Electromagnetic and thermal aspects of radiofrequency field propagation in ultra-high field MRI*. Utrecht University, 2012.

[20] A. L. H. M. W. van Lier, D. O. Brunner, K. P. Pruessmann, D. W. J. Klomp, P. R. Luijten, J. J. W. Lagendijk, and C. A. T. van den Berg. B1+ phase mapping at 7t and its application for in vivo electrical conductivity mapping. *Magnetic resonance in medicine*, 67(2):552–561, 2012.

[21] C. Vuik and D. J. P. Lahaye. Scientific computing lecture notes, september 2014.

[22] A. P. M. Zwamborn. *Scattering by objects with electric contrast*. TU Delft, Delft University of Technology, 1991.